Towards a realistic neutron star binary inspiral: Initial data and multiple orbit evolution in full general relativity

Mark Miller
238-332 Jet Propulsion Laboratory, 4800 Oak Grove Drive, Pasadena, California 91109, USA
and McDonnell Center for the Space Sciences, Department of Physics, Washington University, St. Louis, Missouri 63130, USA

Philip Gressman
Mathematics Department, Princeton University, Princeton, New Jersey 08544, USA
and McDonnell Center for the Space Sciences, Department of Physics, Washington University, St. Louis, Missouri 63130, USA

Wai-Mo Suen
McDonnell Center for the Space Sciences, Department of Physics, Washington University, St. Louis, Missouri 63130, USA
and Physics Department, Chinese University of Hong Kong, Shatin, Hong Kong
(Received 25 June 2003; revised manuscript received 25 November 2003; published 25 March 2004)

This paper reports on our effort in modeling realistic astrophysical neutron star binaries in general relativity. We analyze under what conditions the conformally flat quasiequilibrium (CFQE) approach can generate ''astrophysically relevant'' initial data, by developing an analysis that determines the violation of the CFQE approximation in the evolution of the binary described by the full Einstein theory. We show that the CFQE assumptions significantly violate the Einstein field equations for corotating neutron stars at orbital separations nearly double that of the innermost stable circular orbit (ISCO) separation, thus calling into question the astrophysical relevance of the ISCO determined in the CFQE approach. With the need to start numerical simulations at large orbital separation in mind, we push for stable and long term integrations of the full Einstein equations for the binary neutron star system. We demonstrate the stability of our numerical treatment and analyze the stringent requirements on resolution and size of the computational domain for an accurate simulation of the system.

DOI: 10.1103/PhysRevD.69.064026 PACS number(s): 04.25.Dm, 02.60.Cb, 04.30.Db, 04.40.Dg

I. INTRODUCTION

The analysis of general relativistic binary neutron star processes is an important, yet challenging, endeavor. The importance of understanding these processes is rooted in observational astronomy, both in gravitational wave astronomy and high-energy electromagnetic wave astronomy. Neutron star binaries could be the central engines for some classes of gamma-ray bursts, and they are definitely strong candidates as sources of gravitational radiation detectable by the up and coming generation of gravitational wave detectors such as the Laser Interferometric Gravitational Wave Observatory (LIGO) VIRGO, TAMA, GEO, and Laser Interferometer Space Antenna (LISA). The challenge of understanding binary neutron star processes is rooted in the complexity of both the nonlinear Einstein field equations and the physical properties of the super-nuclear density matter which make up the neutron stars.

Because of the complexity of the binary neutron star system, various levels of approximation have been employed (with various levels of success) as aids in understanding the details of the different stages of the inspiral of comparable mass binary neutron stars, from the quasistationary inspiral stage through to the plunge and merger of the binary stars to the ring-down of the final merged object. These range from the approximation of the structure of the neutron stars themselves (e.g., from point particle to finite sized perfect fluid models and the equations of state with different physical approximations) to the approximation of general relativistic effects (e.g., from Newtonian gravity, to post-Newtonian, to full general relativity). Based on insights from point particle mechanics in general relativity and orbits of finite size bodies in Newtonian gravity, one expects that the early part of the inspiral process will be quasistationary, with the secular (i.e. on time scales larger than the orbital time scale) shrinkage of the orbit driven by gravitational radiation. When the orbit shrinks to a small enough radius (but before touching), there may or may not exist an innermost stable orbit (ISO) beyond which dynamical processes drive the quasistationary inspiral into a plunge phase. Whether there is, in fact, a ''phase change'' from quasistationary inspiral to a plunge phase in the fully relativistic theory, and whether or not this happens before any other (hydrodynamical) dynamical instabilities, is an unsolved problem in full general relativity (see, e.g., [1] for answers in the Newtonian case).

A recent approach for the investigation of the later part of the neutron star inspiral which has been studied in detail [2–11] has drawn much attention. This treatment, which we refer to as the conformally flat quasiequilibrium (CFQE) approach, is a procedure for constructing general relativistic configurations that correspond to compact, equal mass binary neutron stars in a quasiequilibrium, circular orbit. These individual configurations, which we refer to as ''CFQE configurations,'' are by themselves solutions to the constraints of general relativity in $3+1$ form, i.e., the Hamiltonian and momentum constraints. For a given equation of state, each equal mass binary CFQE configuration can be characterized by two parameters: the separation of the two neutron stars and

the baryonic (rest) mass of each of the neutron stars (we only consider equal mass, corotating binary configurations here). Taking the CFQE approximation one step further, one can construct an entire 4-dimensional spacetime by ''gluing'' these configurations together as a time sequence of different CFQE configurations. This construction, which we will refer to as a CFQE sequence, produces a spacetime that solves 5 of the Einstein field equations (4 constraint equations and trace of the extrinsic curvature equation) [2,5]. Since the total baryonic mass will be constant during the inspiral, the CFQE approach takes constant baryonic CFQE sequences as a representation of the evolutionary sequence of the binary neutron star inspiral process; secular evolution of the orbit due to gravitational radiation brings one equilibrium configuration into another with the same rest mass, forming the CFQE sequence [2,5,10,11].

In this CFQE-sequence approach, one finds that for a corotational neutron star binary system (which is the focus of this paper), the Arnowitt-Deser-Misner (ADM) mass of each of the individual CFQE configurations decreases along a constant rest mass CFQE sequence as the separation between the binary stars decreases until a minimum is attained, after which the ADM mass increases as the separation decreases further. Using turning point theorems for exact equilibrium configurations in general relativity [3,12,13], this minimum point signals a secular instability in the evolutionary sequence, and is commonly referred to as the innermost stable circular orbit (ISCO) configuration. In the Newtonian case, it has been shown that this secular instability point is encountered in the evolutionary process *before* any dynamical instability is reached [14].

While it is reasonable to assume that the CFQE approximation holds reasonably well for highly separated neutron stars, it is not clear at which point along the evolutionary sequence the CFQE approximation breaks down. It is certainly not clear whether or not the CFQE-sequence approximation is good for all neutron star separations larger than the ISCO separation, due to the fact that one main assumption in the turning-point theorems [3,12,13] used to interpret these CFQE sequences is the assumption of exact equilibrium. While CFQE configurations are very close to equilibrium for large neutron star separations, they become less so as the separation decreases. Unfortunately, it is exactly the small separation regime, i.e. near the ISCO configuration, in which these theorems are being applied. Also, the CFQE-sequence approximation to full general relativity does not provide an estimate of the error of its solutions, unlike, e.g., the post-Newtonian approach where one can compute the next order post-Newtonian terms to estimate the error of any post-Newtonian approximation.

The fact that each CFQE configuration satisfies the constraints of general relativity suggests the use of these configurations as initial data to full general relativistic calculations. The setting of initial data is obviously an important issue in numerical general relativistic astrophysical simulations. While all initial data configurations satisfying the constraints of general relativity (i.e., the Hamiltonian and momentum constraints) are in principle legitimate initial data sets, they may not be acceptable for the study of coalescence of astrophysical neutron star binaries. In order for the results of the numerical evolutions to be relevant to observations, e.g., the gravitational waves emitted in actual neutron star coalescences, we have to make sure that the initial data actually corresponds to a configuration in an astrophysically realistic inspiral. It is not straightforward how one can go about evaluating the usefulness of the CFQE approach in approximating astrophysically relevant phenomena. We note that while the CFQE approach leads to solutions of the constraint equations, the CFQE-sequence approach is *not* consistent with the full set of Einstein equations.

This paper is divided into four main sections. In Sec. II, we describe our fully consistent general relativistic hydrodynamics code used in this paper. We describe in detail the $3+1$ formulation of the Einstein field equations that we couple to the relativistic hydrodynamics equations, along with details of the gauge conditions and discretization techniques used.

In Sec. III, we describe the CFQE-sequence approximation, whose individual configurations will be used as initial data for our fully consistent general relativistic calculations. We demonstrate that the CFQE-sequence definition of the ISCO for corotating neutron star binaries may not be a relevant concept by showing that if one takes into account the spin energy of the neutron stars when constructing the effective binding energy in the CFQE-sequence approximation, then there is no longer a minimum in the effective binding energy.

In Sec. IV, we analyze the key assumptions of the CFQE-sequence approximation by comparing them with fully general relativistic simulations using CFQE configurations as initial data. We focus on the question of how well the CFQE-sequence approximation for corotating neutron stars approximates full general relativity. This is done by comparing the assumptions in building the CFQE-sequence to fully consistent general relativistic calculations using CFQE configurations as initial data to our numerical evolution code. Specifically, we analyze the conformal flatness assumption and the assumption of the existence of a Killing vector field. We devise a number of invariant measures of these assumptions, and monitor them in our fully consistent, general relativistic simulations. We find that, as expected, the accuracy of the CFQE-sequence approximation increases for increasing neutron star separation. We present a general algorithm for evaluating whether or not any CFQE configuration can be thought of as astrophysically realistic initial data by analyzing how much the CFQE-sequence approximation violates the Einstein field equations. We demonstrate this method by showing that, for any given tolerance, one can find a CFQE configuration whose subsequent evolution in full general relativity will not violate the Einstein field equations within a small fraction of an orbit.

In Sec. V, we analyze the long time scale (i.e. multiple orbits of the binary system) numerical evolutions of CFQE initial data configurations using our general relativistic hydrodynamics code. In particular, we use a CFQE configuration which has a 15% larger proper separation than that of the ISCO CFQE configuration. We analyze the orbital decay rate on multiple orbit time scales. Using care in estimating

the numerical truncation error as well as the errors introduced by placing the computational boundaries at a finite distance from the neutron star binaries, we find that while the computational resources at our disposal are sufficient to get a reasonable handle on the truncation error, the errors introduced by the placement of the boundary of the computational domain can have a significant impact on the dynamics of the neutron star inspiral. We demonstrate that this is true even if the linear dimensions of the computational domain are as large as one half the size of the gravitational waves being emitted, which is a fairly large computational domain by today's numerical relativity standards. We conjecture that presently available computational resources will not allow a unigrid finite difference code to decrease the discretization parameter Δx sufficiently and simultaneously increase the distance from the binary system to the computational domain boundary sufficiently in order to guarantee that the induced numerical errors will not significantly affect the details of the inspiral process. Mesh refinement techniques and/or better outer boundary conditions will be needed in order to accurately simulate the physics on the length scales of the compact object as well as the length scales of the gravitational radiation.

II. FORMULATION AND DISCRETIZATION OF THE EINSTEIN EQUATIONS COUPLED TO A PERFECT FLUID

Our code numerically solves the Einstein field equations coupled to a relativistic perfect fluid. The gravitational degrees of freedom are geometrically encoded in the 4-metric, $g_{\mu\nu}$, which are governed by the Einstein field equations

$$G_{\mu\nu}=8\pi T_{\mu\nu}, \tag{1}$$

where $G_{\mu\nu}$ is the Einstein tensor and $T_{\mu\nu}$ is the stress-energy tensor of the perfect fluid, given as

$$T_{\mu\nu}=\rho h u_\mu u_\nu + P g_{\mu\nu}. \tag{2}$$

Here, we have set the gravitational constant G and the speed of light c to be identically 1. The 4-velocity of the perfect fluid is denoted as u_μ, and ρ, P, and h are the baryonic mass density, pressure, and specific enthalpy, respectively, of the fluid. The equations of motion governing the perfect fluid are the conservation of stress-energy and baryonic mass

$$\begin{aligned}\nabla_\mu T^{\mu\nu}&=0\\ \nabla_\mu(\rho u^\mu)&=0.\end{aligned} \tag{3}$$

These represent five equations governing the five degrees of freedom of the perfect fluid (the mass density, energy density, and velocity). The entire system of equations is closed by choosing an equation of state for the pressure P as a function of the baryonic mass density and internal energy density of the fluid.

A. The Einstein equations in 3+1 form

In order to numerically solve the Einstein field equations, Eq. (1), we must cast the equations as an initial value problem. In order to facilitate this, we introduce a foliation of the spacetime into spacelike hypersurfaces where the coordinate t labels each spacial hypersurface. We furthermore introduce Cartesian coordinates x^i on each spacelike hypersurface. The line element can now be written as

$$ds^2=(\beta^2-\alpha^2)dt^2+2\beta_i\,dt\,dx^i+\gamma_{ij}\,dx^i\,dx^j \tag{4}$$

where the shift vector β^i is a 3-vector defined on each spacelike hypersurface, α is the lapse function, and γ_{ij} is the 3-metric. We denote γ^{ij} as the inverse of the 3-metric γ_{ij}, such that $\gamma^{ij}\gamma_{jk}=\delta^i_k$.

There are many ways to formulate the Einstein equations in an initial value, 3+1 form. The standard "ADM" 3+1 formulation [15] writes the six space-space components of the Einstein equations, Eq. (1), as 12 equations that are first order in time

$$\mathcal{L}_t\gamma_{ij}=-2\alpha K_{ij}+\mathcal{L}_{\vec{\beta}}\gamma_{ij} \tag{5}$$

$$\mathcal{L}_t K_{ij}=\alpha\,{}^{(3)}R_{ij}-2\alpha K^k{}_i K_{jk}+\alpha K K_{ij} \tag{6}$$

$$-\mathcal{D}_i\mathcal{D}_j\alpha+\mathcal{L}_{\vec{\beta}}K_{ij}-\alpha\,{}^{(4)}R_{ij}, \tag{7}$$

where K_{ij} is the extrinsic curvature of a spacelike hypersurface. Here, $\mathcal{L}$ is the Lie derivative operator, $\mathcal{D}_i$ is the covariant derivative operator compatible with the 3-metric γ_{ij}, K is the trace of the extrinsic curvature, ${}^{(3)}R_{ij}$ is the 3-Ricci tensor, while ${}^{(4)}R_{ij}$ are the components of the 4-Ricci tensor that represent the perfect fluid source terms to the Einstein equations. The remaining four Einstein equations are the constraint equations, which are analytically satisfied on each of the spacelike hypersurfaces as long as they are satisfied on the initial slice. The Hamiltonian and momentum constraints are

$${}^{(3)}R+K^2-K_{ij}K^{ij}-2\alpha^2 G^{tt}=0 \tag{8}$$

$$\mathcal{D}_j K^j{}_i-\mathcal{D}_i K-\alpha G^t{}_i=0. \tag{9}$$

While one could base a numerical evolution code on the ADM equations, recent results (both empirical [16,17] and analytical studies [18–20]) indicate that a more suitable choice would be the so-called BSSN formulation [16,17,21]. One feature of this formulation of the Einstein equations is that the 3-metric is decomposed into a conformal factor ϕ and a conformal 3-metric $\tilde{\gamma}_{ij}$ as

$$\gamma_{ij}=e^{4\phi}\tilde{\gamma}_{ij}, \tag{10}$$

where the determinant of the conformal 3-metric $\tilde{\gamma}_{ij}$ is identically 1. Similarly, the extrinsic curvature is decomposed into its trace and trace-free parts

$$K_{ij}=\frac{1}{3}\gamma_{ij}K+e^{4\phi}\tilde{A}_{ij}, \tag{11}$$

where $\tilde{A}_{ij}$ is referred to as the conformal trace-free extrinsic curvature, such that $\tilde{A}_{ij}\tilde{\gamma}^{ij}=0$. In addition to the decompo-

sition of the traditional ADM variables, a key ingredient in the BSSN formulation is the introduction of three new evolved variables, namely the three conformal connection functions $\tilde{\Gamma}^i$

$$\tilde{\Gamma}^i = -\partial_j \tilde{\gamma}^{ij}. \tag{12}$$

The final form of the evolution equations which we use in the numerical evolution of the Einstein field equations is given as

$$\frac{\partial \phi}{\partial t} = -\frac{1}{6}\alpha K + \frac{1}{6}\mathcal{D}_k \beta^k \tag{13}$$

$$\frac{\partial K}{\partial t} = \alpha \tilde{A}^{ij}\tilde{A}_{ij} + \frac{1}{3}\alpha K^2 - \gamma^{ij}\mathcal{D}_i\mathcal{D}_j\alpha + \mathcal{L}_{\vec{\beta}}K + 2\alpha^3 G^{tt} - \alpha^{(4)}R^i_i \tag{14}$$

$$\frac{\partial \tilde{\gamma}_{ij}}{\partial t} = -2\alpha\tilde{A}_{ij} - \frac{2}{3}\tilde{\gamma}_{ij}\mathcal{D}_k\beta^k + e^{-4\phi}\mathcal{L}_{\vec{\beta}}\gamma_{ij} \tag{15}$$

$$\frac{\partial \tilde{A}_{ij}}{\partial t} = \alpha e^{-4\phi\,(3)}R_{ij} - \frac{1}{3}\alpha\tilde{\gamma}_{ij}\left(\tilde{A}_{kl}\tilde{A}^{kl} - \frac{2}{3}K^2\right) + \alpha K\tilde{A}_{ij} - 2\alpha\tilde{A}_{ik}\tilde{A}^k_j - e^{-4\phi}\mathcal{D}_i\mathcal{D}_j\alpha + \frac{1}{3}\tilde{\gamma}_{ij}\mathcal{D}_k\mathcal{D}^k\alpha + e^{-4\phi}\mathcal{L}_{\vec{\beta}}(e^{4\phi}\tilde{A}_{ij}) - \frac{2}{3}\tilde{A}_{ij}\mathcal{D}_k\beta^k - \frac{2}{3}\alpha^3\tilde{\gamma}_{ij}G^{tt} - \alpha e^{-4\phi\,(4)}R_{ij} + \frac{1}{3}\alpha\tilde{\gamma}_{ij}{}^{(4)}R^k_k \tag{16}$$

$$\frac{\partial \tilde{\Gamma}^i}{\partial t} = -2\tilde{A}^{ij}\mathcal{D}_j\alpha - \frac{4}{3}\alpha\tilde{\gamma}^{ij}\mathcal{D}_j K + 12\alpha\tilde{A}^{ij}\mathcal{D}_j\phi - \partial_j\left(e^{4\phi}\mathcal{L}_{\vec{\beta}}\gamma^{ij} + \frac{1}{3}\tilde{\gamma}^{ij}\gamma^{kl}\mathcal{L}_{\vec{\beta}}\gamma_{kl}\right) + 2\alpha\tilde{\Gamma}^i{}_{jk}\tilde{A}^{jk} - 2\alpha^2 e^{4\phi}G^{it}. \tag{17}$$

B. General relativistic hydrodynamics

We also perform a 3+1 decomposition of the hydrodynamics equations, Eq. (3). Note that the 4-velocity u_μ is normalized $u^\mu u_\mu = -1$, so that its components can be written in terms of the three spatial velocity components v^i as

$$\{u^\mu\} = \frac{W}{\alpha}\{1, \alpha v^i - \beta^i\}, \tag{18}$$

where W is the Lorentz factor $W = 1/\sqrt{1-\gamma_{ij}v^i v^j}$. The specific enthalpy, h, is given as

$$h = 1 + \epsilon + P/\rho, \tag{19}$$

where ϵ is the specific internal energy density.

The general relativistic hydrodynamics equations, Eq. (3), can be written in first order, flux conservative form as

$$\partial_t \vec{\mathcal{U}} + \partial_i \vec{F}^i = \vec{S}, \tag{20}$$

where the conservative hydrodynamical variables $\vec{\mathcal{U}}$ are written in terms of the primitive variables $\{\rho, v^i, \epsilon\}$ as

$$\vec{\mathcal{U}} = \begin{bmatrix} D \\ S_j \\ \tau \end{bmatrix} = \begin{bmatrix} \sqrt{\gamma}W\rho \\ \sqrt{\gamma}\rho h W^2 v_j \\ \sqrt{\gamma}(\rho h W^2 - P - W\rho) \end{bmatrix}. \tag{21}$$

The flux vector $\vec{F}^i$ is written as

$$\vec{F}^i = \begin{bmatrix} \alpha(v^i - \beta^i/\alpha)D \\ \alpha((v^i - \beta^i/\alpha)S_j + \sqrt{\gamma}P\,\delta^i_j) \\ \alpha((v^i - \beta^i/\alpha)\tau + \sqrt{\gamma}v^i P) \end{bmatrix}, \tag{22}$$

and the source vector $\vec{S}$ is written as

$$\vec{S} = \begin{bmatrix} 0 \\ \alpha\sqrt{\gamma}T^{\mu\nu}g_{\nu\sigma}\Gamma^\sigma{}_{\mu j} \\ \alpha\sqrt{\gamma}(T^{\mu t}\partial_\mu\alpha - \alpha T^{\mu\nu}\Gamma^t{}_{\mu\nu}) \end{bmatrix}. \tag{23}$$

C. Discretization techniques

We discretize each of the 3 spatial coordinate variables $\{x,y,z\}$ using a constant spacing $\{\Delta x, \Delta y, \Delta z\}$, e.g.,

$$x_i = x_0 + i\Delta x, \quad i = 0, \ldots, n_x - 1. \tag{24}$$

We discretize the time coordinate t as

$$t_{n+1} = t_n + \Delta t \tag{25}$$

where we set $\Delta t = 0.25\Delta x$ for all dynamical simulations performed in this paper.

Due to the fundamental differences in the phenomena being described by the Einstein field equations, Eq. (1), and the relativistic hydrodynamics equations, Eq. (3), the discretization methods that we employ for the two sets of equations are very different. In the case of the Einstein field equations, we expect the dynamical degrees of freedom to remain smooth and continuous. In the case of the relativistic hydrodynamical equations, we know that shocks (discontinuities) can easily form in the physical degrees of freedom. Thus, the discretization method used for the hydrodynamical equations will be more complicated in order to allow for the accurate treatment of shock propagation. The approach we use will be based on a finite differencing scheme employing high resolution shock capturing (HRSC) techniques. In order to use these techniques, a complete knowledge of the characteristic information is needed. We therefore require the eigenstructure of the Jacobian matrices in Eq. (20), namely $\partial \vec{F}^i/\partial\vec{\mathcal{U}}$ for the flux vector $\vec{F}^i$ defined in Eq. (22). This is not a straightforward task, since the flux $\vec{F}^i$ is expressed as a function of both the primitive and evolved hydrodynamical variables.

What we require are a complete set of eigenvectors $[\vec{r}_i]$ and corresponding eigenvalues λ_i such that

$$\left[\frac{\partial \vec{F}^x}{\partial \vec{\mathcal{U}}}\right][\vec{r}_i]=\lambda_i[\vec{r}_i], \quad i=1,\ldots,5. \tag{26}$$

(here, we present the spectral decomposition for the x component of the Jacobian, since the decomposition for the other two spatial components of the Jacobian can be obtained by a straightforward permutation of the spatial coordinates $\{x,y,z\}$). It turns out that the spectral decomposition contains a triply degenerate eigenvalue

$$\lambda_1=\lambda_2=\lambda_3=\alpha v^x-\beta^x. \tag{27}$$

A set of linearly independent vectors that span this degenerate space is given by

$$\vec{r}_1=\left[\frac{\kappa}{hW(\kappa-\rho c_s^2)},v_x,v_y,v_z,1-\frac{\kappa}{hW(\kappa-\rho c_s^2)}\right]^T, \tag{28}$$

$$\vec{r}_2=[Wv_y,h(\gamma_{xy}+2W^2v_xv_y),h(\gamma_{yy}+2W^2v_yv_y), h(\gamma_{yz}+2W^2v_yv_z),v_yW(2Wh-1)]^T, \tag{29}$$

$$\vec{r}_3=[Wv_z,h(\gamma_{xz}+2W^2v_xv_z),h(\gamma_{yz}+2W^2v_yv_z), h(\gamma_{zz}+2W^2v_zv_z),v_zW(2Wh-1)]^T. \tag{30}$$

The other two eigenvalues are given by

$$\lambda_\pm=\frac{\alpha}{1-v^2c_s^2}\{v^x(1-c_s^2) \pm\sqrt{c_s^2(1-v^2)[\gamma^{xx}(1-v^2c_s^2)-v^xv^x(1-c_s^2)]}\}-\beta^x, \tag{31}$$

with corresponding eigenvectors

$$\vec{r}_\pm=\left[1,hW\left(v_x-\frac{v^x-(\lambda_\pm+\beta^x)/\alpha}{\gamma^{xx}-v^x(\lambda_\pm+\beta^x)/\alpha}\right),hWv_y, hWv_z,\frac{hW(\gamma^{xx}-v^xv^x)}{\gamma^{xx}-v^x(\lambda_\pm+\beta^x)/\alpha}-1\right]^T, \tag{32}$$

where the relativistic speed of sound in the fluid c_s is given by (see, e.g., [22])

$$c_s^2=\left.\frac{\partial P}{\partial E}\right|_{\mathcal{S}}=\frac{\chi}{h}+\frac{P}{\rho^2}\frac{\kappa}{h}. \tag{33}$$

We have set $\chi=\partial P/\partial\rho|_\epsilon$ and $\kappa=\partial P/\partial\epsilon|_\rho$. $\mathcal{S}$ is the entropy per particle and E is the total rest energy density which in our case is $E=\rho+\rho\epsilon$. We use the above characteristic information to calculate the numerical fluxes $(\vec{f}^*)^x$ using the piecewise-parabolic method (PPM), described in [23,24]. While the PPM method has been extended to special relativistic applications (see, e.g., [25]), this is the first fully general relativistic application of the method. The discretization of the flux terms in Eq. (20) are written

$$\frac{\partial \vec{F}^x}{\partial x}=\frac{(\vec{f}^*)_{i+1/2}-(\vec{f}^*)_{i-1/2}}{\Delta x}+\mathcal{O}(\Delta x^2). \tag{34}$$

In order to update the discretized hydrodynamical variables, we simply perform a two-step predictor-corrector method, in order that the entire hydrodynamical update is done in a fully second order manner in *both* space and time (modulo the points where the hydrodynamical variables obtain local extrema, where the accuracy of the spatial derivatives drop down to first order in space. This is a well known property of the so-called Godunov schemes; see, e.g., [26]).

As previously stated, since the fields describing the gravitational degrees of freedom are expected to remain smooth, we simply perform centered-in-space discretizing of the spatial derivatives in Eqs. (13)–(17). For discrete time evolution, we use the iterated Crank-Nicholson method [27]. In order to achieve a completely second order method in both space and time for the coupled system of equations (the Einstein field equations and the relativistic hydrodynamics equation), we use the time stepping method described in Fig. 1.

D. Gauge choices and boundary conditions

In the 3+1 initial value formulation of general relativity, one is free to specify the slicing and spatial coordinate conditions by specifying the lapse α and shift β^i, respectively. The code described in the previous subsections has been written allowing for an arbitrary choice of these gauge variables. As described in the next section, each configuration in the CFQE-sequence approximation has a vanishing trace of the extrinsic curvature K. As we would like to compare our full general relativistic simulations to the CFQE-sequence approximation in an invariant manner, it is desirable to use the same slicing condition during the full numerical simulation as that of the CFQE-sequence approximation. To this end, we would like to select the lapse function α such that the trace of the extrinsic curvature K remains 0. Notice that if one sets $\partial K/\partial t=0$ in Eq. (14), then the equation becomes an elliptic equation for the lapse function α. We have thus implemented a multigrid solver [28] for efficiently solving this equation, also known as the maximal slicing condition [29]. However, solving an elliptic equation at every time step can be numerically expensive. We therefore also implement a variant of the so-called ''1+log'' slicing condition for the lapse,

$$\frac{\partial \alpha}{\partial t}=-2\alpha K. \tag{35}$$

Note that this is a completely local condition, and is therefore computationally inexpensive. We use both the maximal slicing condition and the ''1+log'' slicing condition for simulations presented in this paper. For each result, we indicate which slicing condition is used.

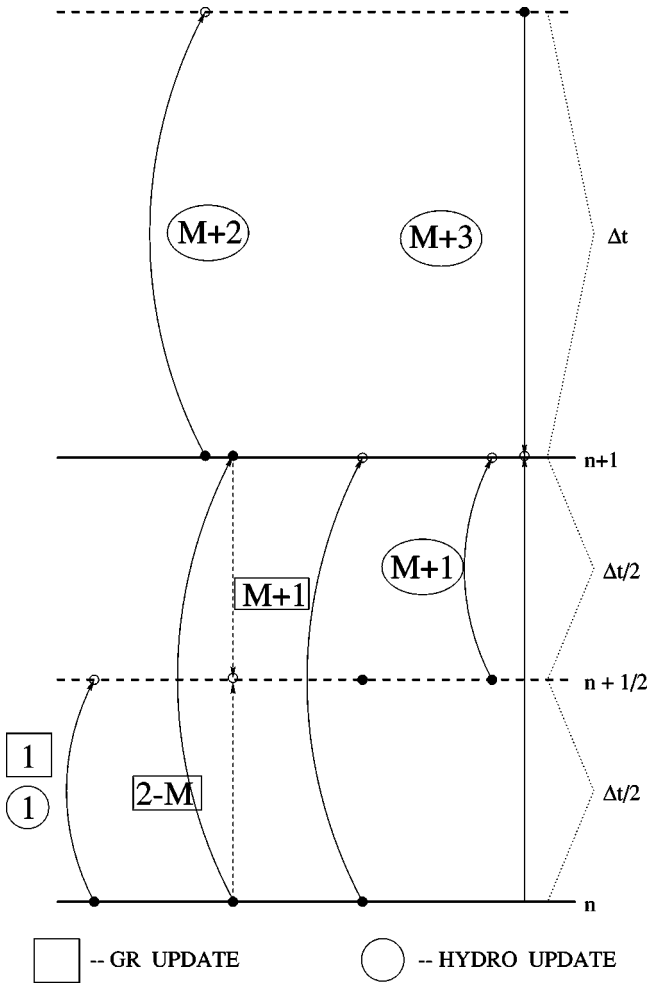

FIG. 1. A representation of the coupling between the hydrodynamic predictor-corrector scheme (circles) and the iterated Crank-Nicholson method used for the integration of the Einstein field equations (squares). **STEP 1:** Simultaneous update of the general relativity and hydrodynamic equations via a Euler-predictor step (first order in time) to the half time step $n+1/2$. **STEP 2 through M:** Update of the general relativity equations via an iterative Crank-Nicholson scheme (second order accurate in time) to the $n+1$ time step, then compute a corrected $n+1/2$ state by averaging the $n+1$ and n states. **STEP M+1:** Simultaneous update of the general relativity equations via a leapfrog step (second order in time) based on the n and $n+1/2$ states, and the hydrodynamics equations via the second half of the Euler-predictor step (first half applied in step 1) using a method of lines. **STEP M+2:** Update of the hydrodynamic equations to a virtual $n+2$ time step via a (first order in time) Euler-corrector step using method of lines. **STEP M+3:** A second order (in time) hydrodynamics update is obtained by averaging the corrected quantities of step $M+2$ at level $n+2$ and the original variables at level n.

For the conditions on the shift, we use a slight modification of the ''Gamma-freezing'' shift equation [30]. Specifically, we implement the first integral form of the hyperbolic Gamma driver (Eq. (46) of Ref. [30]),

$$\frac{\partial \beta^i}{\partial t} = C_1 \tilde{\Gamma}^i - C_2 \beta^i, \tag{36}$$

where we set the constants $C_1 = C_2 = 0.8$ for all numerical simulations in this paper. We find that the Gamma-freezing condition in this modified form, despite its simplicity, results in enhanced stability for the type of problems studied in this paper, and was also very computationally efficient.

The problem of boundary conditions in numerical relativity is only now gaining the attention it deserves [31–35]. Here, we implement a simple, yet empirically stable, boundary condition for the fields describing the gravitational degrees of freedom, Eqs. (13)–(17), due to Alcubierre [30]. Let $f(t,x,y,z)$ represent a field on which we wish to impose this boundary condition in, say, the x face of our computational boundary (the y and z face are similar; averaging this method yields boundary conditions for the edge and corner points of the computational boundary). We take as an ansatz the form for f as $r \to \infty$

$$f(t,x,y,z) \to f_\infty + \frac{u(r-t)}{r} + \frac{w(r+t)}{r}. \tag{37}$$

Taking the derivative of this expression with respect to t and x, and eliminating u and u' yields

$$\frac{x}{r}\frac{\partial f}{\partial t} + \frac{\partial f}{\partial x} + \frac{x}{r^2}(f - f_\infty) = \frac{1}{r^2} H \tag{38}$$

where the function $H = 2xw'$. Equation (38) is finite differenced in a second order fashion to obtain a boundary condition on the field f, where we have interpolated the function H from interior points, assuming a falloff of $\sim 1/r^2$ for H. We adopt this boundary condition for all of the fields describing the gravitational degrees of freedom. The boundary condition used for the hydrodynamical variables is a simple outflow boundary condition. Note that all of the hydrodynamical fields are trivially small at the computational boundary (the atmosphere has a baryonic mass density that is 10^9 times smaller than the central baryonic mass density of the neutron stars), thus the boundary conditions used for these fields are relativity unimportant.

III. THE CONFORMALLY FLAT, QUASIEQUILIBRIUM (CFQE) APPROXIMATION

The mathematical assumptions that go into the conformally flat, quasiequilibrium approximation to general relativity for binary, corotating neutron stars are as follows (for the physical motivation behind the assumptions, see, e.g., [2]).

The physical 3-metric γ_{ij} is assumed to be conformally flat

$$\gamma_{ij} = \psi^4 \delta_{ij}. \tag{39}$$

The Lie derivative of the conformal metric $\psi^{-4}\gamma_{ij}$ with respect to the time variable t is identically zero:

$$\mathcal{L}_t(\psi^{-4}\gamma_{ij}) = 0. \tag{40}$$

The trace of the extrinsic curvature and its time derivative vanishes:

$$K=0 \tag{41}$$

$$\mathcal{L}_t(K)=0. \tag{42}$$

There exists an approximate timelike helical Killing vector field ξ^μ

$$\xi=\left(\frac{\partial}{\partial t}\right)+\Omega\left(\frac{\partial}{\partial \phi}\right) \tag{43}$$

for some constant Ω.

The 4-velocity of the fluid u^μ is proportional to the approximate Killing vector field ξ^μ:

$$u^\mu \sim \xi^\mu. \tag{44}$$

From Eq. (40), the extrinsic curvature K_{ij} takes the form

$$K_{ij}=\frac{1}{2\alpha}\left(\mathcal{D}_i\beta_j+\mathcal{D}_j\beta_i-\frac{2}{3}\gamma_{ij}\mathcal{D}_k\beta^k\right). \tag{45}$$

Using this, along with the assumptions of the conformally flat, quasiequilibrium approximation above, the Hamiltonian constraint, Eq. (8), and the momentum constraints, Eqs. (9), can be written as

$$\partial^i\partial_i\psi+\frac{1}{8\psi^7}\tilde{K}_{ij}\tilde{K}^{ij}+2\pi\psi^5(\rho h W^2-P)=0 \tag{46}$$

and

$$\partial^j\partial_j\beta^i+\frac{1}{3}\partial^i\partial_j\beta^j-\tilde{K}^{ij}\partial_j\left(\frac{2\alpha}{\psi^6}\right)-16\pi\alpha\psi^4\rho h W^2 v^i=0, \tag{47}$$

respectively, where we define the conformal extrinsic curvature $\tilde{K}_{ij}$ as

$$\tilde{K}_{ij}=\psi^2 K_{ij}. \tag{48}$$

Using this form of the Hamiltonian constraint, the maximal slicing condition, $\mathcal{L}_t K=0$, can be written as

$$\partial^i\partial_i(\alpha\psi)-\frac{7\alpha}{8\psi^8}\tilde{K}_{ij}\tilde{K}^{ij}+2\pi\psi^4(2\rho(1+\epsilon)-3P-3\rho h W^2)=0. \tag{49}$$

Since the quasiequilibrium approximation assumes the existence of a timelike Killing vector, we can analytically find the first integral of the relativistic Bernoulli equation, which is simply

$$\frac{u^t}{h}=\text{const.} \tag{50}$$

Along with the normalization condition for the 4-velocity, $u^\mu u_\mu=-1$, this equation can be explicitly written as

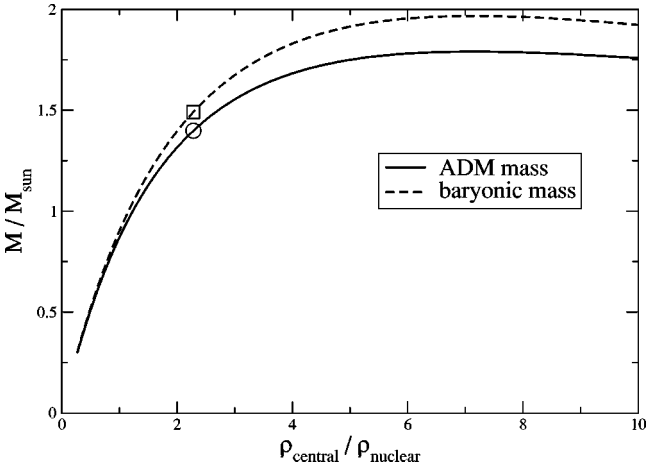

FIG. 2. The ADM mass and baryonic mass (in units of $M_\odot$) as a function of central density (in units of nuclear density) for single, static neutron star configurations. All studies in this paper are done with stars of baryonic mass $1.49M_\odot$ (square). The corresponding ADM mass of this single static configuration is $1.4M_\odot$ (circle).

$$h^2(\alpha^2-\psi^4(\beta^x-y\Omega)^2+(\beta^y+x\Omega)^2+(\beta^z)^2)=\text{const.} \tag{51}$$

A. CFQE configuration

We use the algorithm detailed in [2], along with a parallel multigrid solver, to simultaneously solve the algebraic Bernoulli integral equation, Eq. (51), and the five elliptic equations corresponding to the Hamiltonian constraint [Eq. (46)], the three momentum constraints [Eqs. (47)], and the maximal slicing equation [Eq. (49)], for the conformal factor ψ, the three components of the shift vector β^i, the lapse α, and the matter fields, thus producing a single CFQE configuration. In numerically solving these elliptic equations, we use identical boundary conditions to those in [2]. We have also assumed a polytropic equation of state,

$$P=(\Gamma-1)\rho\epsilon=k\rho^\Gamma, \tag{52}$$

where k is the polytropic constant and Γ is the adiabatic index. The baryonic mass of each neutron star in a CFQE configuration, M_0, is defined as half of the total rest mass of the configuration,

$$M_0=\frac{1}{2}\int d^3x\sqrt{\gamma}\rho W. \tag{53}$$

In this paper, we set $\Gamma=2$ and $k=0.0445(c^2/\rho_n)$, where ρ_n is nuclear density (approximately 2.3×10^{14} g/cm^3). For these values of parameters, a single static neutron star configuration that is stable has a maximum ADM mass of $1.79M_\odot$ and a baryonic mass of $1.97M_\odot$ ($M_\odot$ is 1 solar mass). For the studies in this paper, we use neutron stars with a baryonic mass of $1.49M_\odot$ each, which is approximately 75% that of the maximum stable configuration. The ADM mass of a single static neutron star for this configuration is $1.4M_\odot$ (see Fig. 2).

Once the baryonic mass of each of the stars is fixed, the only remaining degree of freedom in the specification of a

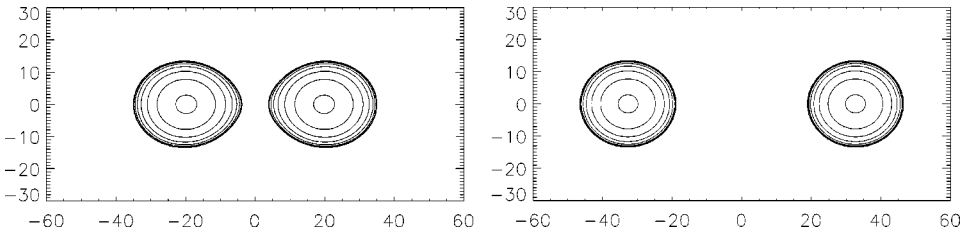

FIG. 3. Contours of the baryonic mass density for two CFQE configurations, taken in the equatorial ($z=0$) plane. The ADM mass of each neutron star in isolation is $1.4M_{\odot}$. The value of the mass density for the first contour is 0.9 that of the maximum mass density of the star, with the others decreasing by a factor of 0.5 each. The CFQE configuration in the left panel has a geodesic separation of $\ell_{1,2}/M_0 = 23.44$ (which is 51.70 km), and the configuration in the right panel has a geodesic separation of $\ell_{1,2}/M_0 = 35.72$ (which is 79.00 km). These configurations represent the smallest and largest separation CFQE configurations that are used as initial data for the fully consistent general relativistic numerical calculations done in this paper.

CFQE corotating configuration is the separation of the two stars. A natural invariant way of specifying the separation of the two neutron stars is to calculate the geodesic distance on the constant t hypersurface between the points in each of the neutron stars that corresponds to the maximum baryonic mass density. Specifically, if x^i_{M1} and x^i_{M2} are the spatial coordinates of the points of maximum baryonic mass density in the first and second star, respectively, then the geodesic whose length will represent the (spatially) invariant separation of the neutron stars is the curve

$$X^i(\lambda), \quad \lambda \in [0,1], \tag{54}$$

where

$$X^i(\lambda=0)=x^i_{M1}, \quad X^i(\lambda=1)=x^i_{M2}, \tag{55}$$

such that

$$\frac{d^2X^i}{d\lambda^2}+\Gamma^i{}_{jk}\frac{dX^j}{d\lambda}\frac{dX^k}{d\lambda}=0. \tag{56}$$

The geodesic distance $\ell_{1,2}$ between the two stars is now defined as

$$\ell_{1,2}=\int_{\lambda=0}^{\lambda=1} d\lambda \sqrt{\gamma_{ij}\frac{dX^i}{d\lambda}\frac{dX^j}{d\lambda}}. \tag{57}$$

We use a relaxation technique for numerically solving the geodesic ODE, Eq. (56), and then use a standard quadrature formula for evaluating the integral for $\ell_{1,2}$, Eq. (57). We choose the discretization for solving Eq. (56) and Eq. (57) to be 10 times as fine as the 3D discretization, and use a third order accurate interpolator to calculate the Christoffel symbols $\Gamma^i{}_{jk}$ from the 3D grid. The maximum baryonic mass points, x^i_{M1} and x^i_{M2}, are located by finding the maximum of a 3D third order accurate interpolation polynomial, the interpolation being centered on the discrete point on the 3D grid that has the largest value of the baryonic mass density in each star.

In Fig. 3, we plot logarithmically spaced contours of the baryonic mass density in the equatorial ($z=0$) plane for two CFQE configurations representing the smallest and largest separations used as initial data for the 3D numerical simulations performed in this paper.

B. The CFQE-sequence approximation

A CFQE sequence is constructed by stringing together several constant baryonic mass CFQE configurations, each configuration differing in only the separation of the neutron stars. The idea is that, due to the fact that the time scale of the gravitational radiation, and thus, that of the orbital decay, is much longer than the orbital time scales, the binary neutron stars are considered to be in ''quasiequilibrium.'' Thus, at any particular time, a binary neutron star system can be described by one particular CFQE configuration; the effect of the gravitational radiation is, over the time scales of one orbit, to alter the configuration to a new CFQE configuration with a slightly smaller separation.

It is typical in CFQE approximation studies to calculate an effective binding energy for each configuration. Following [2], we define the (dimensionless) effective binding energy E_b of a single configuration to be

$$E_b=\frac{M_{ADM}-2M_{NS\infty}}{M_0} \tag{58}$$

where M_{ADM} is the ADM mass of the configuration, and $M_{NS\infty}$ is the ADM mass of a single static neutron star in isolation with rest mass M_0. The usual expression for the ADM mass of an asymptotically flat spatial slice is

$$M_{ADM}=\frac{1}{16\pi}\lim_{r\to\infty}\sum_{i,j=1}^{3}\oint dA\left(\frac{\partial\gamma_{ij}}{\partial x^i}-\frac{\partial\gamma_{ii}}{\partial x^j}\right)N^j, \tag{59}$$

where N^i is the unit outward normal to the sphere of constant radius r, which is the domain of integration. Using the fact that the CFQE configurations are conformally flat, the ADM mass of any configuration reduces to the volume integral

$$M_{ADM}=-\frac{1}{2\pi}\int d^3x(\partial^i\partial_i\psi). \tag{60}$$

In Fig. 4, we plot the effective binding energy E_b as a function of the angular velocity parameter Ω, for a constant

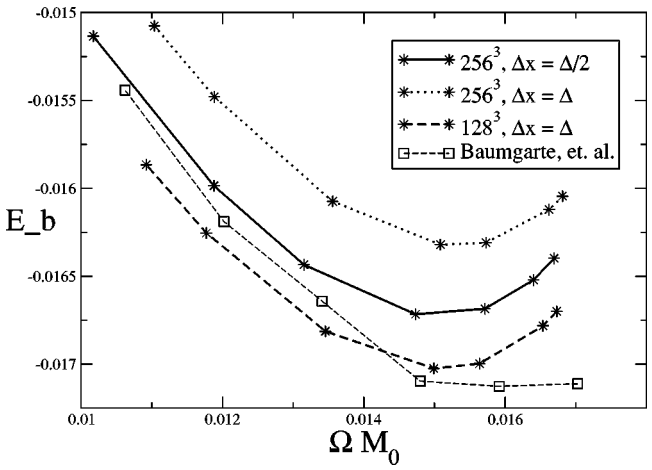

FIG. 4. The effective binding energy E_b as a function of the orbital angular velocity parameter Ω for constant baryonic mass CFQE sequences. The baryonic mass of each of the neutron stars is $1.49M_\odot$. Shown are results for our CFQE configuration solver at different resolutions and outer boundary placements. Tables IV, V, and VI of Ref. [2] were interpolated to obtain the results from Baumgarte *et al.*

baryonic mass CFQE sequence (each star has a baryonic mass of $1.49M_\odot$). The highest value of Ω for each of our calculated CFQE sequences corresponds to a CFQE configuration where the neutron stars are touching. The configuration corresponding to the minimum effective binding energy E_b is the ISCO configuration. It is this point along the CFQE-sequence approximation where the quasiequilibrium configuration goes secularly unstable; the subsequent evolution of the system is thought to enter a ''plunge phase'' where the neutron stars coalesce within an orbital timescale.

Of course, when using a computer code to solve differential equations, results produced at one single resolution are meaningless due to the fact that we have no way of knowing how big the numerical errors are. It is always important to make numerical calculations at different resolutions, in order to be able to assess the numerical errors that are inherent to any discretization. Not only do we have the usual truncation errors (which are due to the fact that higher order terms in the Taylor expansion of functions have been dropped in our finite difference approximation) of any finite difference approximation, we also have boundary errors, as we are solving a set of 5 coupled elliptic equations to arrive at any CFQE configuration. Therefore, we must make at least three numerical experiments in order to assess the effect of both resolution and boundary placement on the numerical results. We show our CFQE configuration results for three combinations of resolution and outer boundary placement, alongside the results obtained by Baumgarte *et al.* [2]. Our CFQE sequence results are in fairly good agreement with those of [2], considering the two terms that are subtracted in the construction of E_b, Eq. (58), are the same to the first two or three significant digits. The resolution used in the two studies are comparable. However, in [2], the number of gridpoints across the neutron star was kept fixed. We, on the other hand, keep (for each sequence calculated) the boundary fixed, and thus have different numbers of gridpoints across the star in each sequence. Notice that, as we both increase the resolution and increase the distance from the center of mass to the boundary of the computational domain, the shape of the curves in Fig. 4 remain roughly the same. In fact, we can perform a Richardson extrapolation on our numerical results by fitting each point on the curve to an error function. For example, we can use the error function

$$(E_b)_{numerical} = (E_b)_{exact} + C_1(\Delta x)^2 + \frac{C_2}{r_{id}^2}, \qquad (61)$$

where $(E_b)_{numerical}$ is the numerical value for the binding energy E_b obtained using a specific discretization Δx and coordinate distance from the center of mass to the outer boundary r_{id} (we use r_{id} to denote this distance in solving the elliptic equations for the CFQE configurations, and we will use r_b to denote the coordinate distance from the center of mass to the outer boundary of the computational domain used during the dynamical evolutions. Of course, we always have $r_{id} \geqslant r_b$). Note that the first nonzero term for the expansion of the boundary error does not contain a $1/r_{id}$ term. This is due to that fact that the boundary conditions we use in solving the elliptic equations for the CFQE configurations, which are identical to those used in [2], are exact to this order. $(E_b)_{exact}$ is the binding energy in the limit as $\Delta x \to 0$ and $r_{id} \to \infty$, i.e. that given by an exact solution to the differential equations. Of course, it is $(E_b)_{exact}$ that we are interested in. We use our three CFQE sequences shown in Fig. 4 to solve for the three unknowns $(E_b)_{exact}$, C_1, and C_2 from Eq. (61). A generous estimate of the total error, which will be used for the size of the error bars, is

$$\text{error} = \max\left\{ |C_1(\Delta x)^2_{\text{best}}|, \left|\frac{C_2}{r_{id}^2{}_{\text{best}}}\right|, \left|C_1(\Delta x)^2_{\text{best}} + \frac{C_2}{r_{id}^2{}_{\text{best}}}\right| \right\}. \qquad (62)$$

The results are plotted in Fig. 5.

C. Neutron star spin corrections to the CFQE-sequence approximation

Note in Fig. 5 that the effective binding energy attains a minimum as the separation between the neutron stars decreases. As explained in the introduction, the CFQE-sequence approximation thus predicts a secular instability at this orbital separation, at which point the evolution of the system will change from quasistationary into a plunge phase, where the neutron stars would merge on timescales of the orbital period. Several types of arguments have been used to support this claim [2,3]. On the one hand, it is intuitively clear that, in the presence of a dissipation mechanism (gravitational waves are slowly dissipating the binding energy of the binary system), if the binding energy would increase with decreasing separation, this would energetically be an unstable situation. There are also turning point theorems [3,12,13] in full nonlinear general relativity which state that

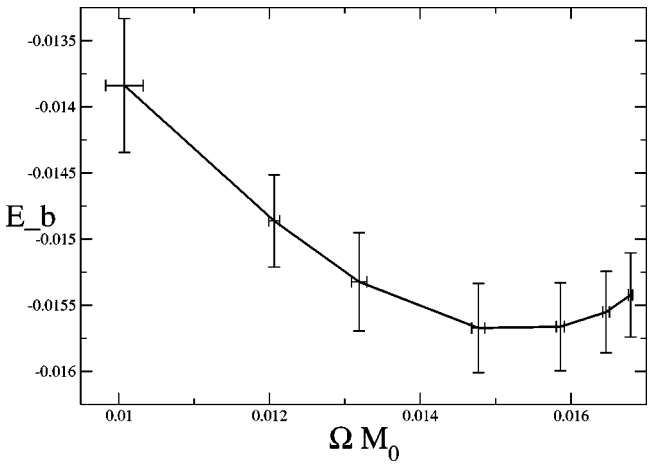

FIG. 5. The effective binding energy E_b as a function of the orbital angular velocity parameter Ω. The data in this plot were obtained by using Richardson extrapolation from the data in Fig. 4. The form of the truncation and boundary error are given by Eq. (61). The error bars were computed using Eq. (62). These results represent what one would obtain in the limit as both $\Delta x \to 0$ and the location of the outer boundary goes to ∞.

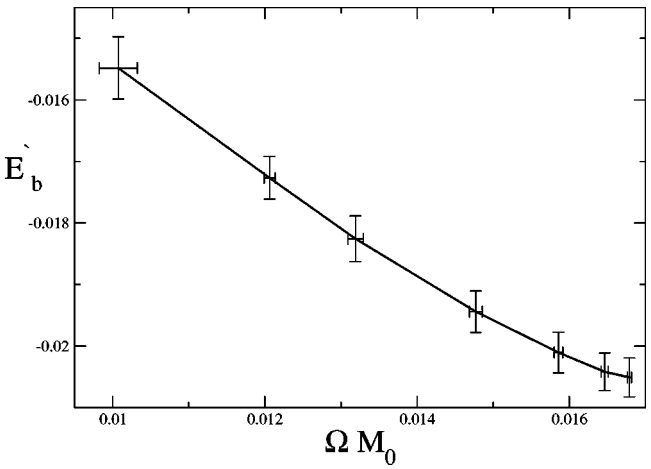

FIG. 6. The effective binding energy E_b', Eq. (63), as a function of the orbital angular velocity parameter Ω. The method for obtaining the data and error bars in this plot are equivalent to those used in producing Fig. 5.

if a sequence of equilibrium configurations attain a minimum in the ADM mass energy, then this equilibrium configuration is secularly unstable. Hence, to the accuracy of the CFQE-sequence approximation, the minimum in Fig. 5 is often referred to as the innermost stable circular orbit (ISCO) configuration.

One problem with the view that these CFQE-sequences somehow approximate fully consistent solutions to the Einstein equations coupled to the relativistic hydrodynamic equations has to do with the spin of the individual neutron stars. Note that in each of the CFQE configurations, the 4-velocity of the fluid is assumed proportional to the timelike helical Killing vector field. The neutron stars are thus spinning at the exact same frequency as the orbital frequency, Ω. The neutron stars are said to be corotating with the orbital motion. However, it has been known for some time that realistic binary neutron stars cannot be tidally locked during the late stages of inspiral (i.e., less than 1000 orbits until the final plunge) [36].

This raises a question: if a CFQE configuration is used as initial data, should we expect the subsequent solution to the Einstein equations to follow the CFQE-sequence approximation, and keep the stars tidally locked as the stars slowly inspiral? In light of the results of [36], the answer must be no. To first order, we would expect the stars to retain approximately the same spin during the dynamical evolutions as is given in the CFQE configuration that was used as initial data.

The resolution of this first question presents a second: what is the status of the ISCO? If the stars do *not*, in fact, stay tidally locked during dynamical evolution, will this affect the location and/or existence of a turning point in the binding energy curve, i.e. the CFQE ISCO configuration? One can gain insight into this question by comparing the spin kinetic energy of relativistic, uniformly rotating neutron stars to the energy scales involved in calculating the binding energy, Eq. (58). To this end, we define a new effective binding energy that explicitly takes the spin kinetic energy of the neutron stars into account:

$$E_b' = \frac{M_{ADM} - 2M_{NS\infty} - 2\Delta M_{RNS\infty}(\Omega)}{M_0} \tag{63}$$

where $\Delta M_{RNS\infty}(\Omega)$ is the difference between the ADM mass of an isolated stationary neutron star with baryonic mass M_0 uniformly rotating with angular velocity Ω and the ADM mass of an isolated static nonrotating neutron star with baryonic mass M_0. Thus, $\Delta M_{RNS\infty}(\Omega)$ represents the spin kinetic energy of a uniformly rotating neutron star rotating with an angular velocity Ω. We plot this new effective binding energy E_b' in Fig. 6. As can be seen, the binding energy where the spin kinetic energy of each of the neutron stars has been manually factored out no longer attains a minimum (the data point with the highest value of Ω corresponds to the CFQE configuration in which the two stars are touching). This indicates that the secular stability of very close binary neutron stars could depend very sensitively on the spin-orbit coupling of the binary system. The two extreme cases, that of tidally locked neutron stars and nonrotating neutron stars, are depicted by Figs. 5 and 6, respectively. The fact that we expect a weak spin-orbit coupling suggests that, in the fully consistent general relativistic hydrodynamics simulations, where we do not expect the neutron stars to remain tidally locked, there may be no turning point and that there may not, in fact, be any ISCO configuration.

IV. COMPARING NUMERICAL EVOLUTION IN FULL GENERAL RELATIVISTIC THEORY WITH THE CFQE-SEQUENCE APPROXIMATION

Using our numerical evolution code described in Sec. II, along with the CFQE configurations described in Sec. III as initial data, we analyze to what degree the CFQE configurations actually correspond to quasiequilibrium configurations

in full general relativity. We do this by computing fully consistent general relativistic evolutions numerically using CFQE configurations as initial data, and comparing the resulting solution of the Einstein field equations with the spacetime obtained by the CFQE approximation. Recall that one major assumption in the CFQE approximation method is that the change of the binary separation is small on time scales less than one orbital period. If the solution to the Einstein equations obtained by using any particular CFQE configuration as initial data deviates significantly from the CFQE-sequence spacetime on suborbital time scales, then that particular CFQE configuration cannot be thought of as representing a quasiequilibrium configuration. Of course, the quasiequilibrium approximation becomes better as the separation of the neutron stars increases. The question then becomes: how close can the neutron stars be before the CFQE approximation breaks down? In this section, we describe a generic method that we subsequently use to answer this question. In short, we use CFQE configurations of differing initial separation as initial data for our fully consistent general relativistic code, and compare the resulting solutions to the Einstein field equations to the CFQE-sequence spacetime in a coordinate independent fashion. The magnitude of these differences, which we find to decrease as the initial separation of the neutron stars increases (as expected), will therefore quantify the degree of failure of the CFQE configurations to be truly quasiequilibrium configurations in full general relativity.

Recall that the CFQE-sequence approximation is done in a maximally sliced ($K=0$) coordinate system. In order to facilitate a meaningful comparison between the fully general relativistic calculation and the CFQE-sequence approach, we adopt this slicing condition for all numerical computations done in this section. Thus, we determine the lapse function α by solving the maximal slicing condition, which is the elliptic equation obtained by setting $\partial K/\partial t$ to 0 in Eq. (14). In order to decrease the computational cost involved in solving this elliptic equation, we only solve the maximal slicing condition every eight time steps. We use "1+log" evolution, Eq. (35), for the lapse α for the timesteps where we do not solve the maximal slicing condition. We have performed several numerical tests where we do, in fact, solve the maximal slicing condition for every time step, and have seen only a negligible affect on the results (in fact, the measures of the violation of the Einstein equations by the CFQE approximation that we find in this section slightly *increase* when we solve the maximal slicing condition for the lapse α at every time step).

In order to meaningfully compare our fully consistent general relativistic simulations with the CFQE-sequence approximation, we must compare quantities that are independent of our choice of coordinates. Since we are using the same slicing condition as that assumed by the CFQE-sequence approximation (namely, maximal slicing), we must compare our numerical results with the CFQE-sequence approximation using quantities that are either fully 4-invariant quantities, or 3-invariant quantities (quantities that are invariant under spatial coordinate transformations). In the following, we will construct measures for comparing our numerically constructed spacetime with the CFQE-sequence spacetime based on both the conformal flatness assumption and the assumption of the existence of a timelike helical Killing vector field. Both of these measures will be exactly zero for the CFQE-sequence spacetime, but will not necessarily be zero for the full solution to the Einstein field equations using CFQE configurations as initial data. The magnitude of these measures will thus quantify the magnitude of the CFQE configuration's failure to correspond to a true quasiequilibrium configuration in full general relativity. In Table I, we show the parameters for the CFQE configurations that are used as initial data for the simulations done in this section.

TABLE I. CFQE configuration parameters used as initial data for fully consistent general relativistic simulations in Sec. IV. For reference, the ISCO configuration has a proper geodesic separation of $\ell_{1,2}=24.0M_0$.

Config.	$M_0/M_\odot$	$\ell_{1,2}/M_0$	J/M_0^2	M_{ADM}/M_0	ΩM_0
NS-1	1.490	23.44	3.770	1.857	0.01547
NS-2	1.490	25.94	3.762	1.857	0.01296
NS-3	1.490	29.78	3.812	1.858	0.01022
NS-4	1.490	35.72	3.934	1.859	0.007460

A. The Killing vector field assumption of the CFQE-sequence approximation

Recall from Sec. III that one assumption of the CFQE-sequence approximation is the existence of an approximate timelike helical Killing vector field, Eq. (43). As we are assuming a corotating matter field, the 4-velocity of the fluid must be proportional to this Killing vector field, Eq. (44). Here, we monitor this quasiequilibrium (QE) assumption in our fully consistent general relativistic numerical calculations.

That the 4-velocity u^a be proportional to a Killing vector field is equivalent to the vanishing of a symmetric, type-(0,2) 4-tensor Q_{ab}

$$Q_{ab}\equiv\nabla_a u_b+\nabla_b u_a+u_a a_b+u_b a_a \tag{64}$$

where $a^a\equiv u^b\nabla_b u^a$ is the 4-acceleration of the fluid (∇_a denotes the covariant derivative operator compatible with the 4-metric g_{ab}). Notice that the quantity $Q_{ab}u^a$ vanishes identically. We can thus monitor the space-space components of Q_{ab} during our simulations as a way of monitoring how well the 4-velocity u^a stays proportional to a Killing vector field. Define Q_{ij} as the projection of Q_{ab} onto the constant t spatial slice:

$$Q_{ij}=P^a{}_i P^b{}_j Q_{ab}=Q_{ab}\left(\frac{\partial}{\partial x^i}\right)^a\left(\frac{\partial}{\partial x^j}\right)^b \tag{65}$$

where $P_{ab}=g_{ab}+n_a n_b$ is the projection operator onto the constant t spatial slices. The unit normal to these spatial slices is $n^a=\alpha t^a+\beta^a$. In our Cartesian coordinates x^i for the spatial slices, the components of Q_{ij} form a 3×3 matrix.

The norm of this matrix, which itself is a coordinate-independent quantity, is the square root of the largest eigenvalue of $Q_{ij}Q^{j}{}_{k}$, where we have raised and lowered 3-indices with the 3-metric. In our case, Q_{ij} is symmetric, and the matrix norm reduces to the largest eigenvalue of Q_{ij} itself. We denote this coordinate-independent value of the norm of Q_{ij} as $|Q_{ij}|$. Note that if the 4-velocity is proportional to an exact Killing vector, $|Q_{ij}|$ will be exactly zero. Of course, in the fully consistent general relativistic treatment, $|Q_{ij}|$ will not vanish. What is required is a sense of the relative size of $|Q_{ij}|$. Notice that in Eq. (64), Q_{ab} is constructed out of only two separate (symmetric) parts, the $\vec{\nabla}\vec{u}$ part and the $\vec{u}\vec{a}$ part. We can therefore naturally normalize $|Q_{ij}|$ by the norms of these two principle parts. If we define

$$Q_{1ab} \equiv \nabla_a u_b + \nabla_b u_a \tag{66}$$

$$Q_{2ab} \equiv u_a a_b + u_b a_a , \tag{67}$$

then a naturally normalized scalar field Q which denotes the deviation from the 4-velocity u^a being proportional to a Killing vector field is

$$Q = \frac{|Q_{ij}|}{\max\{|Q_{1ij}|, |Q_{2ij}|\}}. \tag{68}$$

This normalization provides a measure for the deviation of the 4-velocity u^a from being proportional to a Killing vector field (the QE assumption of the CFQE approach); a value of $Q=0$ signifies that the 4-velocity of the fluid is exactly proportional to a timelike Killing vector, while a value of Q of order unity would signify a significant violation of the QE assumption. The monitoring of Q during a fully consistent general relativistic simulation is then a quantitative measure of the accuracy of the QE approximation. Since Q is meaningful only inside the fluid bodies, a natural global measure of the magnitude of Q is its baryonic mass weighted integral, denoted by $\langle Q \rangle$:

$$\langle Q \rangle = \frac{\int d^3x |Q| \sqrt{\gamma} \rho W}{\int d^3x \sqrt{\gamma} \rho W}, \tag{69}$$

where the integrals are taken to be over the entire spatial slice.

In Fig. 7, we plot $\langle Q \rangle$ as a function of time for a small fraction of an orbit in the fully consistent general relativistic numerical simulations. Configuration NS-1 was used as initial data (see Table I). Various resolutions were used, along with different numbers of gridpoints for the computational domain. As stated in the section where we numerically solved for the CFQE configurations, Sec. III B, it is important to run any simulation at multiple resolutions and boundary placements, in order to assess the magnitude of the boundary error and the finite difference truncation error on the numerical results.

Notice in Fig. 7 that the value of $\langle Q \rangle$ appears to be converging to a curve that attains a maximum value of approximately $\langle Q \rangle = 0.26$ after 1.5% of an orbit ($2\pi/\Omega$ is approximately 1 orbital period). This is quite a fast growth, and a (perhaps unexpectedly) large value attained in such a short time. Recall that $\langle Q \rangle$ is normalized such that a value of $\langle Q \rangle$ of order unity represents a significant failure of the 4-velocity u^a to be proportional to a Killing vector. One reason for this rapid growth has been discussed in Sec. III C: there is no mechanism in the actual evolution to spin up the neutron stars in order that they remain in corotation with the orbital motion. This corotation condition is ''force-fed'' into the CFQE configurations. Of course, one expects that the CFQE-sequence approximation should become better as the separation between the two neutron stars increases. The orbital angular velocity, and thus, the spin of the neutron stars, decreases with increasing separation. Hence, both the gravitational radiation reaction and the error introduced by the artificial spin-up of the individual stars due to the corotation assumption are lessened. These two factors will increase the validity of CFQE approximation for increased neutron star separations.

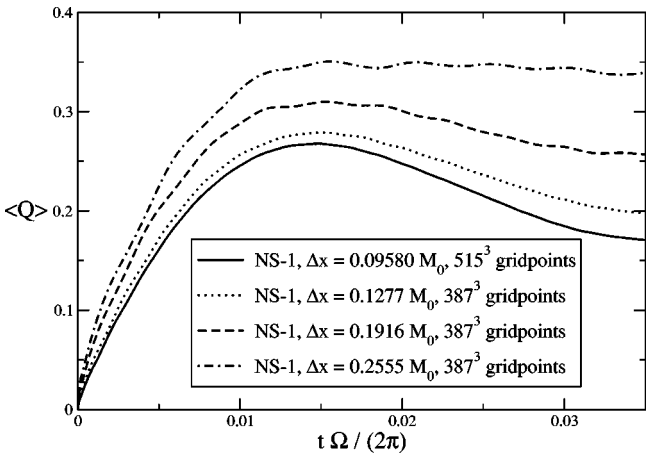

FIG. 7. We plot the quantity $\langle Q \rangle$ [Eq. (69)] as a function of time for fully consistent general relativistic numerical calculations, using CFQE configuration NS-1 as initial data (see Table I). A variety of discretization parameters Δx are used.

In Figs. 8, 9, and 10, we plot $\langle Q \rangle$ as a function of time for increasing neutron star binary separations. Notice that, for each separation, the shape of the curves appear to be converging to something that is qualitatively similar to that of Fig. 7: a quick increase to a maximum value. Also note that this maximum value is, as expected, decreasing for increasing neutron star separation. The best resolution for the maximum initial neutron star separation (NS-4) in Fig. 10 (the solid line) has $\langle Q \rangle$ attaining a maximum value that is already lower than 0.2. A natural question then arises: can one predict how far the initial separation of the neutron stars should be in order that the maximum value of $\langle Q \rangle$ obtained in a short time scale in the consistent general relativistic theory be bounded by some number, say, $\langle Q \rangle = 0.1$? One problem is in the details of the numerical simulations: as the neutron star separation increases, the computational resources demanded by the problem become larger. In other words, for a given fixed amount of computational resources, the ability to resolve each neutron star (e.g., the number of discrete grid-

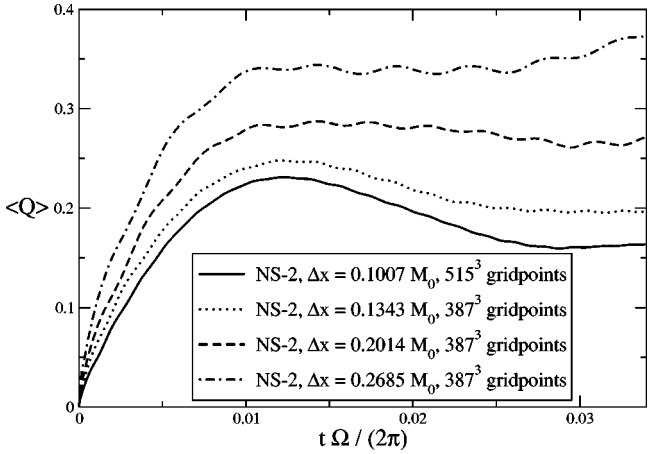

FIG. 8. We plot the quantity $\langle Q\rangle$ [Eq. (69)] as a function of time for fully consistent general relativistic numerical calculations, using CFQE configuration NS-2 as initial data (see Table I). A variety of discretization parameters Δx are used.

points across each star) is diminished as the initial separation of the neutron stars is increased. This can be seen directly when comparing the resolutions used for the simulations performed for Figs. 7, 8, 9, and 10; as the initial neutron star separation is increased in going from CFQE configuration NS-1 to NS-4, the resolution necessarily decreases. These effects can be seen directly in the size of the error bars of Fig. 11, where the maximum value of $\langle Q\rangle$ obtained in the short term general relativistic simulations is plotted as a function of the initial geodesic separation $\ell_{1,2}$. For each data point, we use the maximum value attained by the highest resolution curve (solid line) in each of Figs. 7–10. As always, it is important to estimate the truncation and boundary errors in any numerical calculation. Here, we use an error estimate of the form

$$(\langle Q\rangle_{max})_{numerical}=(\langle Q\rangle_{max})_{exact}+C_1(\Delta x) + C_2(\Delta x)^2+\frac{C_3}{r_b^2}. \quad (70)$$

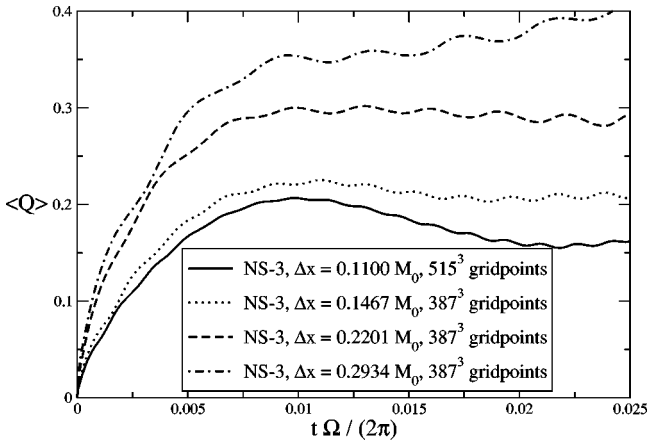

FIG. 9. We plot the quantity $\langle Q\rangle$ [Eq. (69)] as a function of time for fully consistent general relativistic numerical calculations, using CFQE configuration NS-3 as initial data (see Table I). A variety of discretization parameters Δx are used.

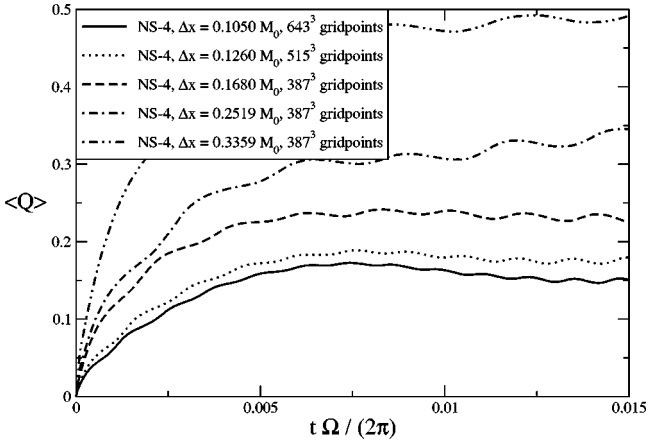

FIG. 10. We plot the quantity $\langle Q\rangle$ [Eq. (69)] as a function of time for fully consistent general relativistic numerical calculations, using CFQE configuration NS-4 as initial data (see Table I). A variety of discretization parameters Δx are used.

Note that we now include a term that is linear in the discretization parameter Δx. This is due to the fact that, although we are using second order methods for the discretization of the Einstein equations, the HRSC methods used for solving the relativistic hydrodynamics equations (described in Sec. II C) are only first order (in space) accurate at points where the hydrodynamical variables obtain a local extrema. Also, while we expect the outer boundary condition on general dynamical simulations to be better represented by a $1/r_b$ error term, we note that in these short time scale simulations, the neutron stars are not even causally connected to the outer boundary. The only boundary error in the calculation is that due to the initial data CFQE configuration solve, whose boundary error decreases as $1/r_b{}^2$. The error bars used in Fig. 11 are computed using the 4 numerical results obtained by varying the resolution and boundary placement for each configuration, and solving Eq. (70) for the constants $(\langle Q\rangle_{max})_{exact}$, C_1, C_2, and C_3. The size of the error bar is then set equal to

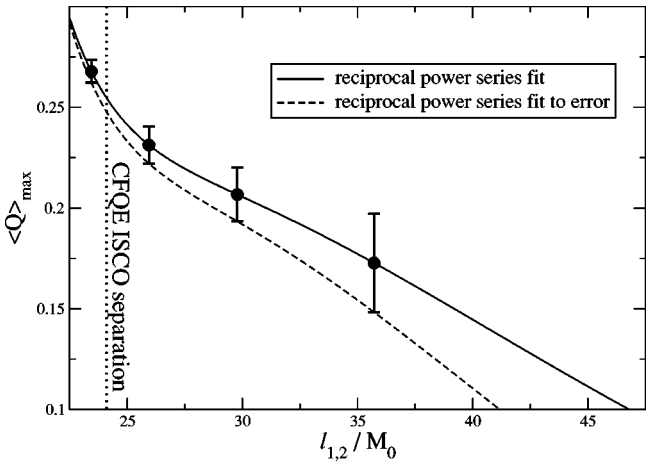

FIG. 11. The maximum value of $\langle Q\rangle$ [Eq. (69)] obtained in our fully consistent general relativistic simulations using different initial CFQE configurations with initial separations $\ell_{1,2}$. The error bars are computed using the error function Eq. (70).

the largest of the absolute value of each individual error term in Eq. (70). With this generous estimate of the error of the maximum value of $\langle Q \rangle$, we can put a lower bound on the initial geodesic separation of the CFQE configuration that must be used as initial data in fully general relativistic simulations such that the Killing vector field assumption is valid, e.g., $\langle Q \rangle < 0.1$. While the value of 0.1 may be somewhat arbitrary (one may desire an even more stringent criterion), the method we use to analyze the CFQE data is quite general. In Fig. 11, we fit a reciprocal power law, $a_1/(\ell_{1,2}) + a_2/(\ell_{1,2})^2 + a_3/(\ell_{1,2})^3 + a_4/(\ell_{1,2})^4$, to both the maximum value obtained in our fully consistent general relativistic calculations, as well as to the lower bound of the estimated error in our calculation. We can see that one would have to use a CFQE configuration initial data set with a geodesic separation between the neutron stars of at least $\ell_{1,2} = 46.8 M_0$ in order for the subsequent solution to the full Einstein field equations to satisfy the Killing field assumption of the CFQE-sequence approximation to 1 part in 10 (this separation parameter could actually be as low as $\ell_{1,2} = 41.2 M_0$, taking into account the errors of our calculations, see Fig. 11). This separation corresponds to roughly twice that of the ISCO separation.

B. The conformal flatness assumption of the CFQE-sequence approximation

One other assumption in the CFQE-sequence approximation is that of conformal flatness (CF). It is often argued that this assumption is, in some sense, equivalent to assuming that there is no gravitational radiation in the configuration. However, the statement that conformally flat configurations have zero gravitational radiation content is very questionable, especially in the case of the CFQE-sequence approximation which is not even consistent with the full set of Einstein equations. Here, we analyze this CF assumption in full general relativity. We start with a CFQE configuration as initial data, and perform fully consistent general relativistic numerical evolutions, monitoring the conformal flatness of the spatial slices. As we are using the same slicing condition (maximal slicing) as that of the CFQE-sequence approximation, we only require a 3-invariant that will allow us to monitor the conformal flatness assumption during the simulations in a coordinate independent way. The 3-Bach tensor is one such 3-invariant. It is defined on the spatial slice as

$$B_{ijk} = 2\mathcal{D}_{[i}\left({}^{(3)}R_{j]k} - \frac{1}{4}\gamma_{j]k}{}^{(3)}R \right), \tag{71}$$

and can be shown to vanish if and only if the 3-metric γ_{ij} is conformally flat. The Cotton-York tensor, H_{ij}, is related to the 3-Bach tensor by

$$H_{ij} = \epsilon^{mn}{}_j B_{mni}, \tag{72}$$

where ϵ_{ijk} is the natural volume element 3-form. We define the scalar H as the matrix norm of the Cotton-York tensor, normalized by the size of the covariant derivative of the 3-Ricci tensor:

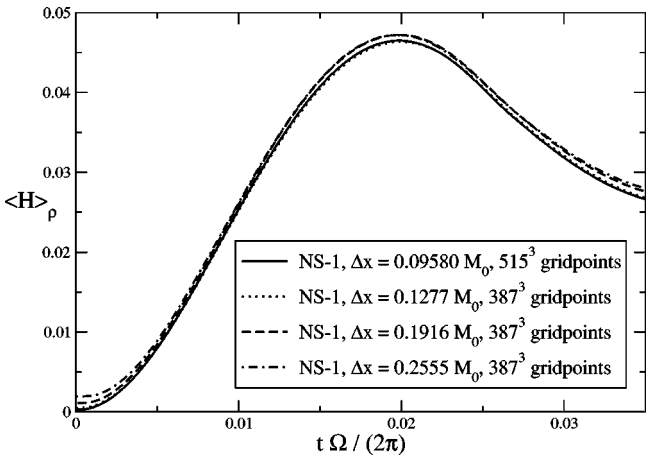

FIG. 12. We plot the quantity $\langle H \rangle_\rho$ [Eq. (74)] as a function of time for fully consistent general relativistic numerical calculations, using CFQE configuration NS-1 as initial data (see Table I). A variety of discretization parameters Δx are used.

$$H = \frac{|H_{mn}|}{\sqrt{\mathcal{D}_i{}^{(3)}R_{jk}\mathcal{D}^{i\,(3)}R^{jk}}}, \tag{73}$$

where, just as in the previous section, $|H_{ij}|$ denotes the matrix norm of the components of H_{ij} in our Cartesian coordinates. Note that H vanishes on conformally flat spatial slices, and is normalized to provide a local measure for determining how much the spatial slice is deviating from conformal flatness. For a global measure, we define the baryonic density weighted norm denoted as $\langle H \rangle_\rho$,

$$\langle H \rangle_\rho = \frac{\int d^3x |H| \sqrt{\gamma}\rho W}{\int d^3x \sqrt{\gamma}\rho W}, \tag{74}$$

where the integrals are taken to be over the entire spatial slice.

In Fig. 12, we analyze the CF assumption of the CFQE-sequence approximation by plotting $\langle H \rangle_\rho$ as a function of time for fully consistent general relativistic simulations. We use for initial data the CFQE configuration NS-1 (see Table I). As it is always imperative to run a numerical code at multiple resolutions and boundary placements to assess the numerical errors, we use a variety of discretizations and grid sizes. Using this measure of the violation of the conformal flatness assumption in the CFQE-sequence approximation, we see that the assumption holds to roughly 1 part in 20, for this initial data. We can also see that this measure, as compared to the measure for the QE assumption [Eq. (69), Fig. 7], is not as sensitive to resolution. In other words, the numerical truncation error for this particular measure is not as large.

Again, we would expect that the CF assumption to be better for larger initial neutron star separation. In Figs 13, 14, and 15, we plot the measure of the violation of the conformal flatness assumption $\langle H \rangle_\rho$, Eq. (74), in our general relativistic simulations using CFQE configurations NS-2, NS-3, and

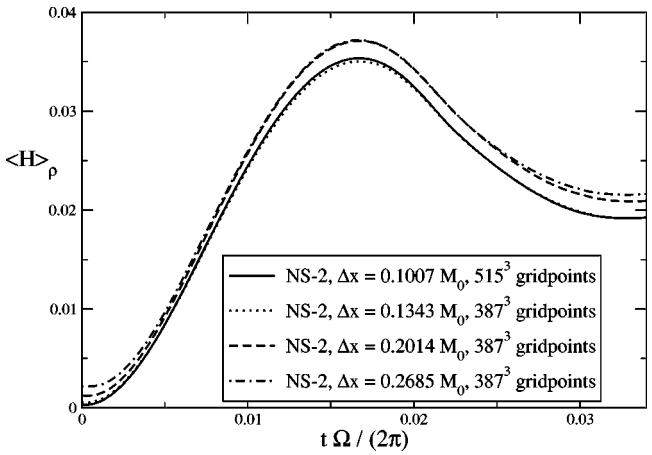

FIG. 13. We plot the quantity $\langle H \rangle_\rho$ [Eq. (74)] as a function of time for fully consistent general relativistic numerical calculations, using CFQE configuration NS-2 as initial data (see Table I). A variety of discretization parameters Δx are used.

NS-4, respectively, as initial data (see Table I). We can see that the violation of the conformal flatness assumption does, in fact, decrease with increasing initial neutron star separation. As with the QE assumption, we can use the results of Figs. 12–15 to predict the initial neutron star separation one would need for a CFQE configuration to satisfy the CF assumption to some prescribed tolerance. For example, we may want to start our general relativistic calculations with initial data that corresponds to a CFQE configuration such that the error in the CF assumption is below one part in 100, as measured by the quantity $\langle H \rangle_\rho$ [Eq. (74)]. In Fig. 16, we plot the maximum value of quantity $\langle H \rangle_\rho$ as a function of initial geodesic separation $\ell_{1,2}$ attained in our fully consistent general relativistic numerical simulations using the four CFQE configurations from Table I as initial data (see Figs. 12–15). Again, we use Eq. (70) and the method described in Sec. IV A to compute the numerical errors (both truncation errors and boundary errors) made in the calculation. We fit an inverse power series function $a_1/(\ell_{1,2}) + a_2/(\ell_{1,2})^2$

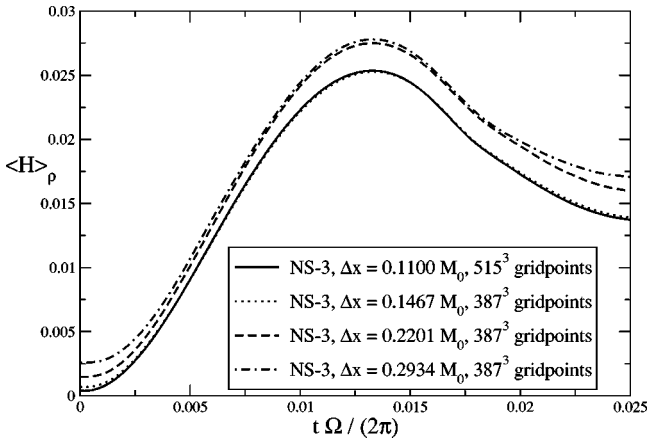

FIG. 14. We plot the quantity $\langle H \rangle_\rho$ [Eq. (74)] as a function of time for fully consistent general relativistic numerical calculations, using CFQE configuration NS-3 as initial data (see Table I). A variety of discretization parameters Δx are used.

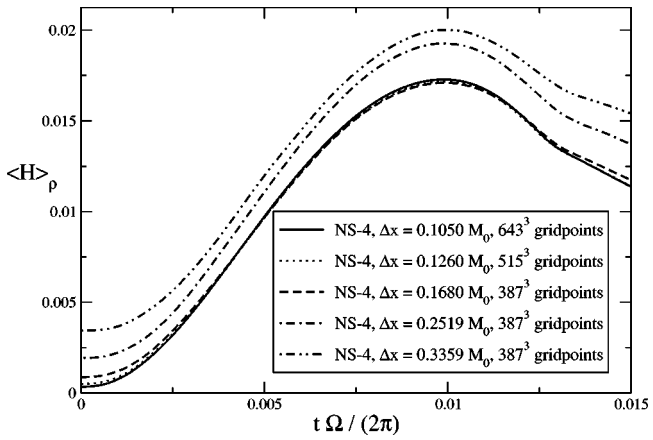

FIG. 15. We plot the quantity $\langle H \rangle_\rho$ [Eq. (74)] as a function of time for fully consistent general relativistic numerical calculations, using CFQE configuration NS-4 as initial data (see Table I). A variety of discretization parameters Δx are used.

$+ a_3/(\ell_{1,2})^3 + a_4/(\ell_{1,2})^4$ to the four data points, as well as to the lower bound of the error, in Fig. 16. As can be seen, one would have to use initial data corresponding to a CFQE configuration with neutron star geodesic separation of approximately $46.7 M_0$ or greater in order for $\langle H \rangle_\rho$ to be 0.01 or less in the subsequent solution to the Einstein field equations coupled to the hydrodynamics equations. Recall from the previous section that this separation would also satisfy the Killing field assumption of the CFQE-sequence approximation to 10%.

V. LONG-TERM GENERAL RELATIVISTIC NUMERICAL SIMULATIONS

In the previous section, we performed many short time scale (suborbital) general relativistic simulations using CFQE configurations as initial data. There, the focus was on determining the intrinsic error in using the CFQE configurations as initial data to model astrophysical neutron star bina-

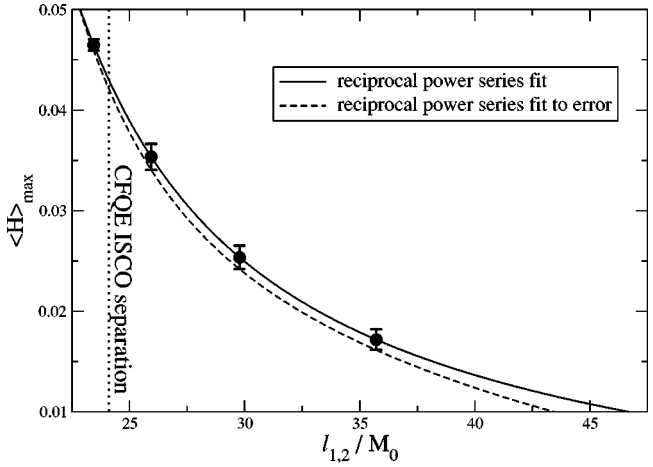

FIG. 16. The maximum value of $\langle H \rangle_\rho$ [Eq. (74)] obtained in our fully consistent general relativistic simulations using different initial CFQE configurations with initial separations $\ell_{1,2}$. The error bars are computed using the error function Eq. (70).

ries. Here, we study the long time scale (i.e., multiple orbital time scale) evolution of the system in order to investigate the stability and accuracy of long term fully general relativistic numerical integrations of the neutron star binary system.

There are several reasons why it is extremely difficult to study large separation binary neutron stars on time scales longer than the orbital period in full numerical relativity in an accurate fashion. One basic reason is apparent from the dynamics of two Newtonian point masses in circular motion. The orbital period T_{orb} increases as the separation D_{sep} of the masses as

$$T_{orb} \sim (D_{sep})^{3/2}. \tag{75}$$

Thus, any simulation of neutron stars with larger separation will naturally have to be run to longer times in order to capture a single orbital period. Also, from the standard quadrapole formula, the energy in gravitational waves E_g emitted per unit time for particles in circular motion decreases with increasing separation D_{sep} as

$$\frac{dE_g}{dt} \sim (D_{sep})^{-5}. \tag{76}$$

Obviously, the time for any simulation to track the orbital motion of compact binaries through the plunge phase to the final merger will be extremely sensitive to the initial separation.

We can get some idea of the computational resources needed to accurately simulate binary neutron stars with initial geodesic proper separations of between $25M_0$ and $35M_0$ (which corresponds to roughly $2.5R_{NS}$ and $4.5R_{NS}$, where R_{NS} is the neutron star radius) from the results of the previous section. In Sec. IV, we performed general relativistic numerical calculations using roughly these separations (see Table I) for only several percent of one orbital period. It took numerical configurations of over 500^3 gridpoints in order to obtain resolutions high enough for a confident prediction of the error of the simulations. In order to perform simulations on orbital time scales, we need to increase the simulation times by two orders of magnitude. While this is already quite difficult, the situation is even more demanding: such a simulation time is much greater than the light crossing time of our computational domain. The neutron stars will no longer be causally disconnected from our dynamical boundary conditions as was the case in the short time scale simulations performed in the previous section. The computational boundary will therefore have a much greater affect on the simulation results if put at the same spatial location. One may need to greatly increase the distance from the center of mass of the system to the computational boundary, but one must be careful not to sacrifice the spatial resolution at the same time.

Preliminary results obtained in [38,40–51] suggest that waveforms calculated from a numerical relativity binary inspiral simulation can be done in an accurate fashion (e.g., with errors less than 10%) only when the extraction radius is approximately one gravitational wavelength λ_g away from the center of mass of the system (for comparison, the NS-4 calculations from the previous section has the outer boundary at only $0.08\lambda_{gw}$). However, gravitational wave extraction is just one aspect of our simulation requirements. Other effects including spacetime dynamics and dynamics of the binary may require the boundary to be even farther away. These facts, coupled with the complexities involved in solving the full Einstein field equations by computer, render the problem of obtaining simulations accurate enough to probe the details of large-separation orbiting binary neutron stars a most difficult one.

TABLE II. The computational domain configurations used for the large time scale binary neutron star general relativistic simulations. All large time scale simulations are performed using initial data corresponding to a CFQE configuration characterized by an orbital angular velocity of $\Omega M_0 = 0.01204$, where the geodesic separation of the neutron stars is $\ell_{1,2} = 27.57M_0$. The gravitational wavelength λ_{gw} corresponding to this configuration is $\lambda_{gw} = \frac{1}{2}(2\pi/\Omega) = 260.9M_0$. r_b denotes the (coordinate) distance from the center of the orbiting binary to the boundary of the computational domain. r_{id} denotes the (coordinate) distance between the center of the orbiting binary to the boundary of the computational domain used in solving for the CFQE initial data configuration.

Configuration	Grid size	$\Delta x/M_0$	r_b/λ_{gw}	r_{id}/λ_{gw}
NS-A	$643\times643\times325$	0.2085	0.257	0.257
NS-B	$323\times323\times165$	0.2085	0.129	0.257
NS-C	$313\times313\times160$	0.2607	0.156	0.160
NS-D	$259\times259\times133$	0.2607	0.129	0.160
NS-E	$163\times163\times85$	0.4171	0.129	0.160

In this section we analyze the numerical evolutions of one particular CFQE initial configuration which has a larger geodesic separation $\ell_{1,2}$ than that of the CFQE ISCO configuration. Specifically, the angular orbital velocity of the CFQE configuration we use exclusively in this section is $\Omega M_0 = 0.01204$. This configuration has a geodesic separation of $\ell_{1,2} = 27.57M_0$, and corresponds to the second smallest Ω data point shown in Fig. 5. According to the study in Sec. IV, this configuration has a violation of the QE and CF assumptions at the 22% and 3% levels, respectively, soon after the evolution starts. We numerically evolve this CFQE initial data configuration using our fully consistent general relativistic treatment. The gauge conditions used for these simulations are the "1+log" equation for the lapse α [Eq. (35)] and Eq. (36) for the shift vector β^i. There is no need to use maximal slicing in this section as comparing to the CFQE sequence is no longer the point.

In Table II, we list the properties of the various computational domains, varying both the resolution and outer boundary placement, used for our long time scale numerical evolutions. Our numerical implementation allows us to use a different location for the outer boundary of the computational domain for our initial data solve of the CFQE configuration as that used for the dynamical evolution. We denote r_{id} as the shortest coordinate distance between the center of our computational domain and the computational boundary of our cubical domain used in solving the initial data problem for the CFQE configuration. We denote r_b as the shortest coordinate distance between the center of our computational

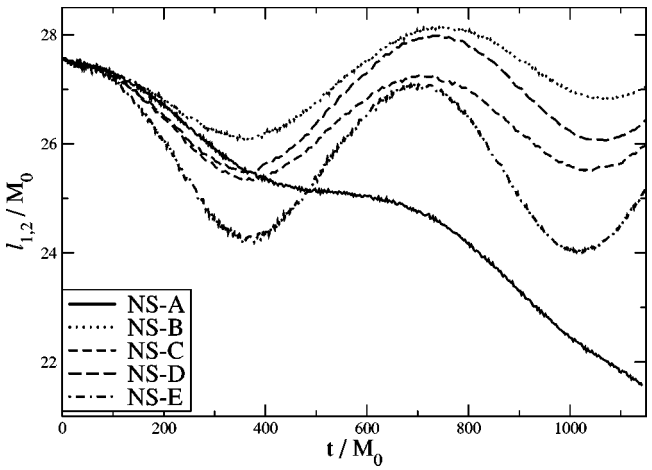

FIG. 17. We plot the evolution of the geodesic distance between the maximum rest mass density of the two neutron stars as a function of coordinate time for various resolutions and outer boundary placements (see Table II for configuration specifications).

domain and the computational boundary of our cubical domain used in our fully consistent general relativistic numerical simulations. Note that in Table II, the number of grid points refers to that used in the full dynamical evolution. For those computational domains where $r_{id} > r_b$, we have used the same resolution Δx with a larger number of grid points to solve for the CFQE initial data configuration.

In Fig. 17, we plot the geodesic separation $\ell_{1,2}$ as a function of coordinate time t using this initial data for the various computational domains listed in Table II. Qualitatively, we observe a number of interesting features. First of all, note that all of the simulations in Fig. 17 display an eccentricity in the orbit. Some level of eccentricity is expected due to the fact that the CFQE configuration is constructed with the explicit assumption that the time derivative of the separation $\ell_{1,2}$ exactly vanishes, as argued in [52–55]. That is, the assumption of the radial velocity of the binaries to be exactly zero instantaneously (which is done by assuming the existence of a timelike helical Killing vector field in the construction of CFQE configurations) is not consistent with the astrophysically relevant scenario of quasicircular binary evolution, where the magnitude of the radial velocity, while small, never vanishes. One can obtain some idea regarding the level of orbital eccentricity intrinsic to CFQE configurations by analyzing the point-particle dynamics in the post-Newtonian approximation [54]. In [54], it is shown in the context of the post$^{9/2}$-Newtonian approximation that if the assumption of circular motion is used to construct the initial conditions (that is, the conditions $\dot{r}=0$ and $\ddot{r}=0$ are used to specify the initial conditions), then the resulting orbit will have a nonzero eccentricity whose value depends on the initial separation.

Ideally, we would like to directly compare our general relativistic results for the eccentricity of the orbits apparent in Fig. 17 with the post-Newtonian results in [54]. The reason we are unable to do this at the present time is obvious from Fig. 17. Note the large difference between the eccentricity for computational domain configuration NS-A as compared to the other configurations. In fact, it is obvious from Fig. 17 that the NS-A configuration is qualitatively different from the other configurations. Recall that all configurations NS-A through NS-E use the same CFQE configuration as initial data; note from Table II that the only parameters that differ in producing the results from Fig. 17 are the spatial resolution of the discretized computational domain, the location of the outer boundary of the computational domain during numerical evolution where the dynamical boundary conditions are imposed, and the location of the outer boundary of the computational domain used in solving for the CFQE initial data configuration. A cursory study of Table II reveals the major difference between computational domain configuration NS-A and the others, namely, the location of the outer boundary r_b of the computational domain during numerical evolution. The boundary distance r_b of the computational domain configuration NS-A is slightly larger than 1/4 of the gravitational wavelength λ_{gw} characterized by the CFQE initial data configuration, while all of the other configurations have $r_b \leqslant 0.156\lambda_{gw}$.

We must always quantify the errors of any numerical calculation. Here, our numerical errors originate from two distinct sources. The first source of error is the truncation error associated with our discretization parameter Δx, while the second source of error is induced by the outer boundary conditions imposed on our numerical calculation. While the behavior of the truncation error is well understood (it is a local error which scales as an integer power of the discretization parameter Δx), the assessment of the effect of the boundary conditions is not as straightforward. Theoretically, one could place the outer boundary of the computational domain sufficiently far away so that the outer boundary condition would not be causally connected to the compact objects, and thus would have no effect on them during numerical evolution. However, this is not a practical solution, due to the limitations of computational resources (especially for a unigrid code; adaptive mesh refinement could be used in this direction). As our outer boundary *is* causally connected to the neutron stars in our simulations, we must attempt to assess the errors introduced by the outer boundary conditions in our numerical simulations. We assume that the error induced by the outer boundary conditions can be expanded in terms of powers of $1/r_b$, and that the error goes to 0 as $r_b \to 0$. We therefore assume an error function for the eccentricity e as

$$e_n = e_{exact} + C_1(\Delta x) + C_2(\Delta x)^2 + \frac{C_3}{r_b} + \frac{C_4}{r_b^2}. \qquad (77)$$

where e_n denotes the measured value of eccentricity from our numerical solution using discretization parameter Δx and outer boundary location r_b. Using the definition of eccentricity defined in [54] in which the eccentricity of the orbit is calculated from the orbital separation as a function of time, we compute the eccentricity associated with each simulation shown in Fig. 17. We find that $(e_n)_{NS-A}=0.0124$, $(e_n)_{NS-B}=0.0327$, $(e_n)_{NS-C}=0.0397$, $(e_n)_{NS-D}=0.0434$, and $(e_n)_{NS-E}=0.0605$. We can then solve for the unknown quantities e_{exact}, C_1, C_2, C_3, and C_4 in Eq. (77). We find

that the Richardson extrapolated value of the eccentricity is $e_{exact}=-0.127$, and that the leading error terms for the truncation error and boundary error are $C_1\Delta x=0.067$ and $C_3/r_b=0.11$, respectively. Above and beyond the fact that the Richardson extrapolated value of the eccentricity e_{exact} is negative, the obvious sign that we are not in the convergence regime [i.e., that the higher order terms neglected in the error expansion of Eq. (77) are not relatively small] is that $|e_{exact}-e_n|$ is larger than the error terms in Eq. (77). As the computational resources available at the present time do not currently allow us to use our unigrid code to simultaneously decrease the discretization parameter Δx further and increase the distance r_b from the center of mass to the outer boundary, we must admit that we can, at this time, make no definite conclusion as to the inherent eccentricity in CFQE configurations used as initial data in numerical relativity. However, the prospect of being able to determine this point in the near future is good; we can expect both mesh refinement techniques and better outer boundary conditions to greatly aid in reducing the errors induced by the outer boundary in our numerical calculations.

A. Orbital decay rate

Recall from Secs. III B and III C that the binding energies E_b and E_b' [Eqs. (58) and (63), respectively] shown in Figs. 5 and 6 represent the binding energy of each neutron star binary CFQE configuration as a function of geodesic separation $\ell_{1,2}$ (the orbital angular velocity Ω is monotonically increasing with decreasing geodesic separation $\ell_{1,2}$). In the CFQE-sequence approximation, this binding energy is slowly converted to gravitational wave energy, and Figs. 5 and 6 tell us how much gravitational radiation energy is produced for changes in geodesic separation. We can approximate the rate of energy loss at any specific point in this sequence using the standard quadrupole formula (see, e.g., [39]), which reduces to

$$\frac{dE_{gw}}{dt}=\frac{128}{5}M^2R^4\Omega^6 \tag{78}$$

for two point particles of mass M in circular orbit with radius R and orbital angular velocity Ω. We interpolate the data represented in Figs. 5 and 6 with a cubic spline to obtain the effective binding energies E_b [Eq. (58)] and E_b' [Eq. (63)] as a function of geodesic separation $\ell_{1,2}$. We can then easily find $dE_b/d\ell_{1,2}$ as a function of geodesic separation. An estimate of the time rate of change of geodesic separations is then

$$\frac{d\ell_{1,2}}{dt}=\frac{dE_{gw}/dt}{dE_b/d\ell_{1,2}}, \tag{79}$$

which can be numerically integrated to produce the geodesic separation $\ell_{1,2}$ as a function of time predicted from the CFQE-sequence approximation. We plot these functions in Fig. 18, along with results from our fully consistent general relativistic calculation NS-A and NS-B.

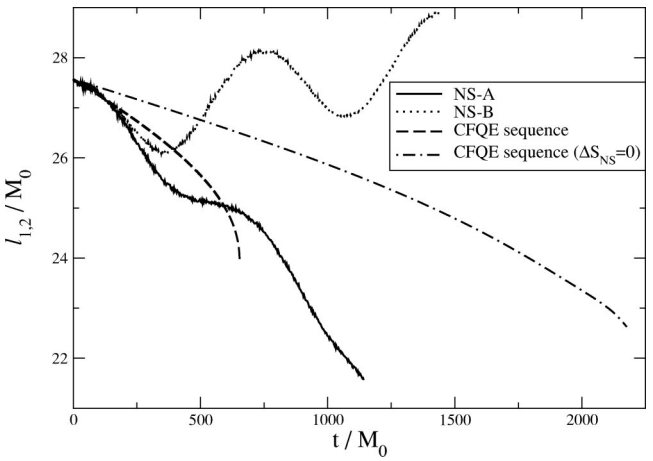

FIG. 18. The geodesic separation $\ell_{1,2}$ as a function of time. Shown are the results from our fully consistent general relativistic calculation NS-A and NS-B (see Table II). Also shown are predictions from the CFQE-sequence approximation, i.e. the curve obtained by numerically integrating Eq. (79). The curve labeled "CFQE sequence" was constructed using the standard definition of binding energy, Eq. (58) (see Fig. 5), and is terminated at the CFQE ISCO point ($\ell_{1,2}/M_0=24.0$). The curve labeled "CFQE sequence ($\Delta S_{NS}=0$)" was constructed using the binding energy E_b', Eq. (63), where the neutron star spin remains constant throughout the entire CFQE sequence (see Fig. 6 and the discussion in Sec. III C), and is terminated at the neutron star touching point ($\ell_{1,2}/M_0=22.6$).

Note that the standard CFQE-sequence prediction of the evolution of the geodesic separation $\ell_{1,2}$, labeled "CFQE sequence" in Fig. 18, terminates at a neutron star geodesic separation $\ell_{1,2}=24.0M_0$, whereas the modified CFQE-sequence prediction, labeled "CFQE sequence ($\Delta S_{NS}=0$)," terminates at a smaller geodesic separation of $\ell_{1,2}=22.6M_0$. This is due to the fact that the standard effective binding energy E_b defined by Eq. (58) actually attains a minimum before the neutron stars touch (see Fig. 5), whereas the effective binding energy for the CFQE sequence where the spin of the neutron stars do not change [E_b' defined by Eq. (63)] is monotonically decreasing as the neutron star separation decreases, right through to the point where the neutron stars are touching (see Fig. 6). Therefore, the first "CFQE-sequence" prediction in Fig. 18 terminates at this minimum point (defined as the ISCO configuration of the sequence), whereas the second "CFQE sequence ($\Delta S_{NS}=0$)" prediction in the figure terminates at the CFQE configuration where the neutron stars are touching. One might expect that a full solution to the Einstein equations using a CFQE configuration as initial data might, in fact, have an evolution of the geodesic separation of the neutron star binaries $\ell_{1,2}$ that would lie somewhere in between the two CFQE-sequence approximations shown in Fig. 18. After all, these two CFQE-sequence approximations represent the extreme cases of the evolution of the neutron star spin; the first represents complete tidal locking during the entire evolution, the second represents absolutely no change in the spin state of the individual neutron stars during the entire evolution. Of course, the actual solution to the full Einstein equations

would be expected to couple, to some amount, the increasing orbital angular frequency of the binary neutron stars to the spin of the individual stars. The magnitude of this coupling would determine which of the two CFQE-sequence approximations shown in Fig. 18 would be considered to be ''more'' correct. It is exactly this question which could be answered with our fully consistent general relativistic calculations. However, in Fig. 18 we once again see the dramatic effect of the outer boundary conditions on our numerical simulations. Note that computational domain configurations used in the calculations NS-A and NS-B have the same spatial resolution $\Delta x = 0.2085 M_0$ and outer boundary location $r_{id} = 0.257 \lambda_{gw}$ used for solving the CFQE initial data configuration. The only difference between the configurations NS-A and NS-B is the outer boundary placement used during the dynamical evolution: the outer boundary of the computational domain used during numerical simulation NS-A is twice as far away from the center of mass as that used in simulation NS-B. One may be tempted to conclude that the calculation NS-A could be said to be ''more correct'' than NS-B, since the outer boundary is located farther away for the NS-A configuration. However, one must be careful when trying to apply physical intuition to numerical results that are not in the convergence regime. In this case, for instance, there is no reason to believe that the error induced by the outer boundary on our calculation is a monotonic function of r_b (whereas, e.g., it is true in general that the truncation error is monotonic in Δx as $\Delta x \rightarrow 0$). Due to the wave nature of the gravitational radiation being emitted by the binary neutron stars, the boundary errors could have an oscillating component. This makes it even more difficult to try to do a Richardson extrapolation type of error analysis in realistic compact object simulations in numerical relativity.

While it should be expected that the extraction of gravitational radiation for a numerically generated spacetime could be highly sensitive to the location of the outer boundary (see [38]), there have been, up to now, no results showing what effect the outer boundary conditions can have on the details of the orbits of compact binaries on time scales larger than one orbital period. Here, we see that the dynamical outer boundary conditions can, and do, significantly affect the orbital parameters of compact binaries during numerical evolution.

VI. CONCLUSIONS

To date, the only fully general relativistic simulations of corotating binary, $\Gamma = 2$ polytropes is [37]. The study in [37] differs from the present study in several important ways. One basic difference is that while we focus on the capability of simulating astrophysical realistic neutron star binaries, Ref. [37] focuses on the dynamics of the final merger of the two neutron stars. Thus, the initial data used in [37] are CFQE configurations either at ISCO separation, or closer than ISCO separation (ISCO separation here means simply the neutron star separation of the unique configuration that corresponds to a minimum of the binding energy in the constant rest mass CFQE-sequence, e.g., in Fig. 5). Also, in the study [37], it was found necessary to manually decrease the orbital angular momentum of each CFQE configuration at the level of several percent, in order to precipitate the binary merger more quickly. Complementary to that approach, we are trying to use numerical relativity as a tool to assess the fidelity of the CFQE-sequence approximation itself. We found that in order to perform simulations of the neutron star binary systems compatible with realistic astrophysical scenarios, one must perform simulations using initial data at a distance considerably larger than the ISCO separation when using corotating CFQE configurations as initial data.

We have outlined a generic method for analyzing the regime of validity of the CFQE-sequence approximation and have applied this method to the case of equal mass, corotating binary neutron stars. We have found that, for corotating neutron stars, the violation of the timelike helical Killing vector field existence assumption was an order of magnitude larger than the violation of the assumption of conformal flatness. Specifically, we have demonstrated that initial data specified by a CFQE configuration with neutron stars having an initial geodesic separation of less than $47 M_0$ (which is slightly more than 6 neutron star radii, or roughly twice the ISCO configuration separation) would produce a solution to the Einstein field equations that violates the Killing vector field assumption by more than 1 part in 10; the conformal flatness assumption would be violated by more than 1 part in 100. We thus conclude that, in the corotating case, the CFQE-sequence approximation for neutron star separations of $47 M_0$ and less violates the Einstein field equations at a level larger than 10%, and thus numerical simulations starting with similar CFQE configurations as initial data cannot, therefore, be considered as approximating a realistic neutron star binary inspiral.

We note that the violations of the assumptions of the CFQE-sequence approximation that we observe in our general relativistic calculations for the corotating binary systems occur on time scales that are two orders of magnitude shorter than the orbital time scale. We suspect that this may be due to interactions between the spin assumption of the individual neutron stars (the corotating assumption) and the CFQE assumptions. We have shown that the characteristic shape of the effective binding energy curve within the CFQE approximation is highly sensitive to the spin kinetic energy of the individual neutron stars. We have shown that if we subtract out the spin kinetic energy of the neutron stars in the construction of the effective binding energy (which approximates the case where the neutron star spin does not increase as the orbital angular velocity increases), then the resulting binding energy curve will have no minimum, and thus the CFQE-sequence approximation would not predict the existence of an ISCO configuration. We speculate that specifying neutron stars with irrotational spin states in the CFQE-sequence approximation may yield a smaller violation of the Einstein field equations for a fixed neutron star separation. The analysis we have developed in this paper can be used for a detailed investigation of this effect. More interestingly, the analysis we have developed might provide a way to determine a spin state most consistent with the CFQE approximations, and hence provide a more realistic set of initial data

that can be used to start simulations at a smaller initial separations.

We have shown that, for our specific neutron star models, we require a resolution of approximately $\Delta x = 0.1 M_0$ in order to adequately resolve the neutron stars (''adequately resolve'' here refers to verifying that we are in the convergence regime through an appropriate Richardson extrapolation technique; this is a much more stringent condition than has been typically used in numerical relativity studies to date involving neutron stars and black holes). This resolution scale is over three orders of magnitude smaller than the characteristic wavelength of the gravitational radiation emitted during the last five to ten orbits of the neutron star inspiral process.

We have also shown that the location of the outer boundary of the computational domain can have a significant impact on the details of the evolution of the compact objects on time scales of the orbital period. Specifically, we have seen that changing the linear dimensions of our computational domain from $0.3\lambda_{gw}$ to $0.5\lambda_{gw}$ can significantly impact the dynamics of binary neutron stars during the first several orbits. This should serve as a warning to the numerical relativity community studying simulations of compact binaries with the hope of extracting gravitational wave information: not only will the outer boundary inhibit the actual process of extracting the gravitational waves, but they also directly affect the sources of the gravitational waves themselves. While our dynamical boundary conditions are not the best choice, and a more consistent treatment, e.g. constraint preserving boundary conditions, would most likely improve the situation, it may be that numerical relativists will be forced to push the outer boundary of the computational domain to the ''local wave zone'' (which in this case means $r_b \geqslant \lambda_{gw}$) in order to provide realistic gravitational waveforms suitable for use as templates in gravitational wave detectors.

Unfortunately, this makes the numerical study of orbiting compact objects in numerical relativity particularly hard. Note that every time we increase the resolution in our 3D simulations by a factor of two, keeping the outer boundary r_b fixed, we must use 16 times the amount of computational resources to perform any particular simulation. Also, every time we increase the outer boundary distance r_b by a factor of two, we must use 8 times the amount of computational resources. Therefore, if we wanted to simultaneously increase both the resolution and the outer boundary distance by a factor of 2, we would require over two orders of magnitude more computational resources. While we have shown in this paper that it is possible to track the details of finite sized compact objects in full numerical relativity, what remains is to be able to do so in such a way that all of the numerical errors (both truncation and boundary errors) can be demonstrated to be small over a time scale of several orbital periods. This will be an extremely challenging task, given the current level of computational resources available. It may be necessary to employ mesh refinement in order to accurately simulate all of the physical degrees of freedom that we are interested in.

ACKNOWLEDGMENTS

It is a pleasure to thank Abhay Ashtekar, Comer Duncan, David Garfinkle, Lee Lindblom, David Meier, Peter Miller, Thierry Mora, Masaru Shibata, Kip Thorne, and Clifford Will for useful discussions and comments. We also thank Nikolaos Stergioulas for providing us with code for calculating the ADM mass of stationary, uniformly rotating polytropic stars. Our application code which solves the Einstein equations coupled to the relativistic hydrodynamic equations, along with our various multigrid elliptic solvers, uses the CACTUS Computational Toolkit [56] for parallelization and high performance I/O. Financial support for this research has been provided by the ASC project (NSF Phy 99-79985) and the Jet Propulsion Laboratory (account 100581-A.C.02) under contract with the National Aeronautics and Space Administration. Computational resource support has been provided by the NSF NRAC projects MCA02N022 and MCA93S025, and the NAS at Ames, NASA.

[1] F.A. Rasio and S.L. Shapiro, Astrophys. J. **401**, 226 (1992).
[2] T.W. Baumgarte, G.B. Cook, M.A. Scheel, S.L. Shapiro, and S.A. Teukolsky, Phys. Rev. D **57**, 7299 (1998).
[3] T.W. Baumgarte, G.B. Cook, M.A. Scheel, S.L. Shapiro, and S.A. Teukolsky, Phys. Rev. D **57**, 6181 (1998).
[4] S. Bonazzola, E. Gourgoulhon, and J.-A. Marck, Phys. Rev. D **56**, 7740 (1997).
[5] E. Gourgoulhon, P. Grandclement, K. Taniguchi, J. Marck, and S. Bonazzola, Phys. Rev. D **63**, 064029 (2001).
[6] P. Marronetti, G.J. Mathews, and J.R. Wilson, Phys. Rev. D **60**, 087301 (1999).
[7] M. Shibata, Phys. Rev. D **58**, 024012 (1998).
[8] S. Teukolsky, Astrophys. J. **504**, 442 (1998).
[9] H.-J. Yo, T. Baumgarte, and S. Shapiro, Phys. Rev. D **63**, 064035 (2001).
[10] M.D. Duez, T.W. Baumgarte, and S.L. Shapiro, Phys. Rev. D **63**, 084030 (2001).
[11] M.D. Duez, T.W. Baumgarte, S.L. Shapiro, M. Shibata, and K. Uryu, Phys. Rev. D **65**, 024016 (2002).
[12] R.D. Sorkin, Astrophys. J. **257**, 847 (1982).
[13] J.L. Friedman, J.R. Ipser, and R.D. Sorkin, Astrophys. J. **325**, 722 (1988).
[14] D. Lai, F.A. Rasio, and S.L. Shapiro, Astrophys. J., Suppl. Ser. **88**, 205 (1993).
[15] R. Arnowitt, S. Deser, and C. W. Misner, in *Gravitation: An Introduction to Current Research*, edited by L. Witten (Wiley, New York, 1962), pp. 227–265.
[16] T.W. Baumgarte and S.L. Shapiro, Phys. Rev. D **59**, 024007 (1999).
[17] M. Alcubierre, B. Brügmann, T. Dramlitsch, J. Font, P. Papadopoulos, E. Seidel, N. Stergioulas, and R. Takahashi, Phys. Rev. D **62**, 044034 (2000).
[18] M. Alcubierre, G. Allen, B. Brügmann, E. Seidel, and W.-M. Suen, Phys. Rev. D **62**, 124011 (2000).

[19] M. Miller, gr-qc/0008017.
[20] O. Sarbach, G. Calabrese, J. Pullin, and M. Tiglio, Phys. Rev. D **66**, 064002 (2002).
[21] M. Shibata and T. Nakamura, Phys. Rev. D **52**, 5428 (1995).
[22] L.D. Landau and E.M. Lifshitz, *The Classical Theory of Fields* (Pergamon, Oxford, 1975).
[23] P. Woodward and P. Collela, J. Comput. Phys. **54**, 115 (1984).
[24] P. Collela and P.R. Woodward, J. Comput. Phys. **54**, 174 (1984).
[25] J.M. Martí and E. Müller, J. Comput. Phys. **123**, 1 (1996).
[26] C. Hirsch, *Numerical Computation of Internal and External Flows* (Wiley-Interscience, New York, 1992).
[27] S. Teukolsky, Phys. Rev. D **61**, 087501 (2000).
[28] A. Brandt and B. Diskin, *Multigrid Solvers on Decomposed Domains* (American Mathematical Society, Providence, RI, 1994).
[29] J. York, in *Sources of Gravitational Radiation*, edited by L. Smarr (Cambridge University Press, Cambridge, England, 1979).
[30] M. Alcubierre, B. Brügmann, P. Diener, M. Koppitz, D. Pollney, E. Seidel, and R. Takahashi (unpublished).
[31] H. Friedrich and G. Nagy, Commun. Math. Phys. **201**, 619 (1999).
[32] B. Szilagyi, B. Schmidt, and J. Winicour, Phys. Rev. D **65**, 064015 (2002).
[33] G. Calabrese, L. Lehner, and M. Tiglio, Phys. Rev. D **65**, 104031 (2002).
[34] J. Bardeen and L. Buchman, Phys. Rev. D **65**, 064037 (2002).
[35] B. Szilagyi and J. Winicour, Phys. Rev. D **68**, 041501(R) (2003).
[36] L. Bildsten and C. Cutler, Astrophys. J. **400**, 175 (1992).
[37] M. Shibata and K. Uryu, Phys. Rev. D **61**, 064001 (2000).
[38] M. Shibata and K. Uryu, Phys. Rev. D **64**, 104017 (2001).
[39] R.M. Wald, *General Relativity* (The University of Chicago Press, Chicago, 1984).
[40] J.R. Wilson and G.J. Mathews, Phys. Rev. Lett. **75**, 4161 (1995).
[41] J.R. Wilson, G.J. Mathews, and P. Marronetti, Phys. Rev. D **54**, 1317 (1996).
[42] G. Mathews and J. Wilson, Astrophys. J. **482**, 929 (1997).
[43] P. Marronetti, G.J. Mathews, and J.R. Wilson, Phys. Rev. D **58**, 107503 (1998).
[44] M. Shibata, Phys. Rev. D **55**, 6019 (1997).
[45] D. Lai, Phys. Rev. Lett. **76**, 4878 (1996).
[46] A.G. Wiseman, Phys. Rev. Lett. **79**, 1189 (1997).
[47] J.C. Lombardi, F.A. Rasio, and S.L. Shapiro, Phys. Rev. D **56**, 3416 (1997).
[48] P.R. Brady and S.A. Hughes, Phys. Rev. Lett. **79**, 1186 (1997).
[49] E.E. Flanagan, Phys. Rev. D **58**, 124030 (1998).
[50] M. Shibata, T.W. Baumgarte, and S.L. Shapiro, Phys. Rev. D **58**, 023002 (1998).
[51] M. Shibata, Phys. Rev. D **60**, 104052 (1999).
[52] T. Mora and C.M. Will, Phys. Rev. D **66**, 101501(R) (2002).
[53] C.W. Lincoln and C.M. Will, Phys. Rev. D **42**, 1123 (1990).
[54] M. Miller, gr-qc/0305024.
[55] K. Thorne, Rev. Mod. Phys. **52**, 299 (1980).
[56] Cactus, *http://www.cactuscode.org*.